Novel Syntheses of Thermoelectric and Nanostructured Materials and a System for Purifying and Sorting Metallic and Semiconducting Single-Walled Carbon Nanotubes in a Mixed-Tube Suspension

by

Su (Ike) Chih Chi

A dissertation submitted to The Johns Hopkins University in conformity with the requirements for the degree of Doctor of Philosophy

Abstract

The integration of materials science and engineering at the nanoscale has significant impact in many areas of science and technology. In this dissertation, I will present novel syntheses of lanthanum telluride thermoelectric materials, vertically-aligned nanowires, and nanoporous nickel membranes. I will also present a method that can collect industrially relevant quantity of purified and sorted metallic and semiconducting single-walled carbon nanotubes (SWCNTs) in a mixed-carbon nanotubes suspension by AC dielectrophoresis.

In the Chapter 1: A Novel Approach to Synthesize Lanthanum Telluride Thermoelectric Materials, I will report on the electrochemical synthesis of lanthanum telluride thin films. The electrodeposition of lanthanum telluride thin films is performed in a room-temperature ionic liquid, 1-ethyl-3-methylimidazolium bromide (EMIB), in ambient conditions. This novel procedure can serve as an alternative means of simple, inexpensive, and laboratory-environment friendly methods to synthesize rare-earth telluride thermoelectric materials that were difficult to make in aqueous solution. Characterization of the morphologies and chemical compositions of the deposited films using scanning electron microscopy (SEM), x-ray diffractometry (XRD), and energy-dispersive x-ray analysis (EDAX) will be presented. The Seebeck coefficient and

electrical resistivity of deposited lanthanum telluride thin films will also be presented and compared with those of current state-of-the-art thermoelectric materials.

In the Chapter 2: Synthesis and Characterization of Vertically-aligned Gold Nanowires Arrays Ferromagnetic Composite Films, I will report on the electrochemical synthesis of films composed of vertically-aligned gold nanowire arrays in ferromagnetic matrices (nickel and iron). This process involves first electrodepositing the Au nanowire arrays within commercially available anodic aluminum oxide (AAO) nanoporous membranes. After dissolving the templates, the ferromagnetic matrices are grown around the nanowires to produce the two-phase nanocomposites.

In the Chapter 3: A Novel Approach to the Synthesis of Nanochanneled Nickel Films, I will report on an innovative technique to fabricate nickel nanochanneled membranes. This procedure involves transferring and imprinting the nanoporous arrays of the AAO membranes to a nickel film using a template-guided electrochemical etching technique. A detailed discussion of these processing techniques will be shown along with the characterization of the morphology of nickel nanochanneled membranes.

Lastly, in the Chapter 4: Purification and Refinement of Single-Walled Carbon Nanotubes (SWCNTs) by AC Dielectrophoresis (DEP), a continuous flow device for purifying and sorting metallic and semiconducting SWCNTs from an initially random mixture of SWCNTs in suspension using AC dielectrophoresis is reported. The separation of two electronic types of SWCNTs takes advantage of the large difference of the relative dielectric constants between metallic and semiconducting SWCNTs with respect to the suspension, resulting in both a difference in magnitude and direction of a dielectrophoretic force imposed on the SWCNTs. This work presents a significant

advancement in nanotubes purification in a facile and scalable manner, and can therefore significantly increase the feasibility of manufacturing reliable SWCNT-based nanoelectronic devices. A detailed discussion of the sorting techniques will be presented along with the fabrication of a dielectrophoretic force utilized microfluidic lab-on-a-chip device that can continuously refine and collect metallic and nonmetallic nanoparticles at industrially relevant processing rates. The effectiveness of the device is characterized using resonant Raman and ultraviolet–visible-near infrared (UV-Vis-NIR) spectroscopy analysis on sorted samples.

To my parents and my sister for their unconditional supports and sacrifices during the years of my Ph.D. study

Acknowledgments

Firstly, I would like to thank my parents, Hsien-Ling Wei and Kuo-Ching Chi and my sister, Dr. Sabrina Su-Li Chi for their unconditional supports and sacrifices throughout the years of my Ph.D. study.

I would like to especially thank to my research advisor, Prof. Robert C. Cammarata for his guidance and constant support on my research works as well as many regarding life in general. I am especially grateful to my committee members: Prof. Jonah Erlebacher and Prof. En Ma of Department of Materials Science and Engineering and Prof. Chia-Ling Chien of Department of Physics and Astronomy and and Prof. Howard Fairbrother of Department of Chemistry for their kindness and useful discussions during my thesis defense. I am also very grateful to the funding support from Prof. Chia-Ling Chien of Department of Physics and Astronomy.

I would also like to thank current and previous Cammarata group's members: Mr. Stephen Farias, Mr. Austin Young, Mr. Nicholas Dee, and Mr. Rustin Golnabi for their kindly supports on my research works in general throughout the years of my Ph.D. study in Baltimore, MD. I would like to especially thank to Mr. Stephen Farias again for his role as my initial mentor and then numerous valuable discussions on my research works as well as regarding life in general.

I would like to thank Ms. Danru Qu of Johns Hopkins University for the initial collaborations of the carbon nanotubes separation project. I am also very indebted to her kindness and unconditional supports for conducting many property measurements and helping me with material syntheses. Without her help, my thesis work would become much more problematic. I would also like to thank Dr. Sunxiang Huang and Mr. Mingen Li of Johns Hopkins University for preforming many material's property measurements on the samples I synthesized.

I would like to appreciatively thank to Mr. Yu-Ja Huang of Johns Hopkins University for training me the techniques of microfabrication and coaching me valuable knowledge regarding microfluidic devices made of polydimethylsiloxane (PDMS). I am very thankful to Dr. Maya Zayats of Johns Hopkins University to get me the access of the cleanroom in her lab. I am also gratefully thank my officemate, Mr. Samuel Rosenthal, for many helpful discussions on the technical issues of my thesis works as well as regarding life in general throughout the last two years of my Ph.D. study.

I would like to gratefully thank Mr. Ming-Ling Yeh of Johns Hopkins University for performing Seebeck coefficient and electrical resistance measurements of the electrodeposited Lanthanum Telluride films and many useful discussions regarding my research works throughout the years of my Ph.D. study. I am very grateful to Dr. Kailiang Ren, Dr. Weiguo Huang, and Mr. Yu Liu of Johns Hopkins University for many valuable discussions on my technical issues as well as regarding life in general. My lunch would not be the same without your guys.

I would like to thank Mr. Ian McCue of Johns Hopkins University for many useful discussions regarding the preparation and the chemistry of room temperature ionic

liquids. I would also like to thank Prof. Todd C. Hufnagel of Johns Hopkins University for valuable discussions regarding X-ray diffraction pattern of the electrodeposited Lanthanum Telluride films. Ms. Mantong Zhao of Johns Hopkins University is also acknowledged for many useful discussions regarding X-ray diffraction pattern in general.

I would like to acknowledge Dr. Shaka Prokes, Dr. Joshua Caldwell, and Dr. Konrad Bussmann of Naval Research Laboratory and Dr. Natalia Drichko of Johns Hopkins University for performing the resonant Raman studies of separated single-walled carbon nanotubes (SWCNTs) from the static system. Ms. Sarvenaz Sarabipour of Johns Hopkins University and Dr. Jesse Placone of currently University of Maryland are acknowledged for allowing me to have access to the equipment of their lab. Dr. Yong Ren of Johns Hopkins University is acknowledged for getting me the access of the ultraviolet-visible (UV-Vis) spectrophotometry of his lab. I would like to gratefully thank to Dr. Xuan Jiang and Mr. Deng Pan for their kindness for helping me regarding the knowledge of biological materials throughout the first two years of my Ph.D. study.

I would like to gratefully thank Mr. Mark Koontz of Johns Hopkins University for assistance with the scanning electron microscopy (SEM) as well as regarding lots of hardware troubleshooting in general throughout the years of my Ph.D. study. I also want to thank Ms. Marge Weaver and Ms. Dorothy Reagle for their wholehearted supports throughout the years of my Ph.D. study. I would also like to gratefully thank Ms. Jeanine Majewski for her kindness to make my thesis defense pleasantly happen.

Contents

List of Tables

List of Figures

Chapter 1

A Novel Approach to Synthesize Lanthanum Telluride Thermoelectric Materials

1.1 Introduction

This section is an adapted reproduction from *Mater. Res. Soc. Symp. Proc.* Vol. 1543 (2013). Copyright 2013, Materials Research Society.

Rare-earth elements and their telluride alloys have attracted significant attention because of their potential applications in thermoelectrics, electronics, and optoelectronics.[1-2] In particular, lanthanum and lanthanum telluride alloys are of interest because lanthanum is used in large quantities in nickel metal hydride (NiMH) rechargeable batteries for hybrid automobiles. The negative electrode (cathode) in NiMH batteries is a mixture of metal hydrides, one of which is typically lanthanum hydride. The active material at the cathode is hydrogen, which is stored in the metal hydride structure.[3] A Toyota Prius battery requires 10 to 15 kg (22 to 33 lb) of lanthanum.[4-5] Lanthanum can also be used to make the infrared-absorbing glass in night vision goggles. High quality camera and telescope lenses contain lanthanum oxide (La_2O_3) making use of its high refractive index and low dispersion.[6] In addition, May and co-workers reported that nanostructured bulk lanthanum telluride ($La_{3-x}Te_4$, $0 < x \leq \frac{1}{3}$) produced by

mechanical ball-milling exceeded the figure of merit (ZT) of 1 at high temperatures near 1300K.[7-8] LaTe and La_2Te_3 are good candidates for photoconductive and photovoltaic cells applications.[9-10] $LaTe_2$ and $LaTe_3$ are n-type semiconductors having unique electronic properties.[9-11]

Since the increased thermoelectric efficiency of nanostructured materials are due to the enhancement of phonon scattering introduced by quantum confinement, thin films (2-D systems) and nanowires (1-D systems) also have generated significant scientific and technological interest.[12,13-15] Here, I report on the electrochemical synthesis of lanthanum telluride thin films. Electrochemical deposition is a very attractive process for synthesizing thin films of compound semiconductors on metallic surfaces.[16] The thickness of thin films can be controlled by deposition duration. An advantage of this technique is that it is a simple, inexpensive, and laboratory-environment friendly synthesis methods for telluride based thermoelectric materials.

Producing thick rare-earth telluride films can be very material consuming when using physical vapor deposition methods such as sputtering or evaporation, but films of several microns thickness can be produced in a few hours using electrochemical deposition. In addition, variations in the deposition potential or solution concentration can provide different molar ratios of La-Te. It is important to note that aqueous solutions are not preferred for lanthanum alloy electrodeposition because hydrogen evolution can occur before the deposition of metals. Recently, room-temperature ionic liquids (RTILs) have attracted significant attention in the electrodeposition of rare-earth metals in ambient conditions.[17-18] Here, I report on the electrodeposition of lanthanum and lanthanum telluride alloys in a ionic liquid, 1-ethyl-3-methylimidazolium bromide

(EMIB), which has the advantages of good cathodic stability, low hygroscopy, and low reactivity with oxygen and moisture.

1.1.1 Thermoelectric Figure of Merit (ZT)

Thermoelectric generators (TEGs) can be treated as Carnot cycle engines, but instead of a gas or liquid, the working fluid is electrons.[19-21] The maximum efficiency of an thermoelectric generator is related to both the product of the Carnot efficiency and a thermoelectric material properties depended parameter known as figure of merit (*ZT*).

$$\eta_{max} = \frac{T_H - T_C}{T_H} \frac{\sqrt{1+ZT}-1}{\sqrt{1+ZT}+\frac{T_C}{T_H}}, \tag{1.1}$$

where η_{max} is the maximum efficiency of the thermoelectric generator, T_H is the temperature at the hot junction, and T_C is the temperature where the surface is getting cooled.[19-21] The thermoelectric figure of merit (*ZT*) is a dimensionless parameter that is related to three material transport properties. *ZT* is written as

$$ZT = \frac{S^2}{\rho\kappa} T, \tag{1.2}$$

where *S* is the Seebeck coefficient (μV/K), ρ is the electrical resistivity (mΩ-cm), κ is the thermal conductivity (W/mK), and *T* is the absolute operating temperature (K).[19-21] Sometimes, the performance of a thermoelectric material can be referred to its power

factor in thermoelectric generation applications. The power factor, P (W M^{-1} K^{-2}), can be expressed as

$$P = \frac{S^2}{\rho}, \tag{1.3}$$

where S is the Seebeck coefficient (μV/K) and ρ is the electrical resistivity (mΩ-cm).[19-21] The thermal conductivity, κ, can be expressed as $\kappa_{el} + \kappa_{lat}$, where κ_{el} is the electronic thermal conductivity and κ_{lat} is the lattice thermal conductivity.[22] Thermoelectric materials with high power factors can generate more energy from the thermoelectric effect, but they are not necessarily very efficient. This can be understood using Fourier's law of thermal conduction, for the heat flow $q = -\kappa \frac{dT}{dx}$. For a given heat flux, when a thermoelectric material has a large thermal gradient from that heat flux and the thermal conductivity of that material is low, the material is considered thermoelectric efficient.[19-20]

The Seebeck coefficient, S, is a material property that characterizes the response of the net diffusion of electrons to a thermal gradient. Mathematically, the coefficient is represented as

$$S = \frac{V}{\Delta T}, \tag{1.4}$$

where V is the measured voltage change across a material when a thermal gradient is applied to the material and ΔT is the temperature difference due to the thermal gradient.[19-

[20] The Seebeck coefficient is negative when the material is an n-type semiconductor because the direction of electric current is opposite to the direction of thermal diffusion. On the other hand, when a material is a p-type semiconductor, its Seebeck coefficient is positive because the direction of electric current is the same as the direction of thermal diffusion.[19-20]

Since all three parameters (Seebeck coefficient, electrical resistivity, and thermal conductivity) that appear in the figure of merit (*ZT*) are functions of carrier concentration, it is important to understand the interrelationship between carrier concentration and the three material transport properties. Electrical resistivity is an important parameter to determine the thermoelectric properties of materials. Metals usually have a low electrical resistivity, while that of insulators is high and that of semiconductors is intermediate between that of metals and insulators. In most textbooks and references, electrical resistivity is usually reported and discussed by its inverse parameters, electrical conductivity, which is represented as,

$$\frac{1}{\rho} = \sigma, \tag{1.5}$$

where ρ is electrical resistivity and σ is electrical conductivity.

Referring to Figure 1.1 reprinted from *CRC Handbook of Thermoelectrics: Macro to Nano* edited by D. M. Rowe, one can understand that in order to optimizing the power factor of a thermoelectric material, it is necessary to find the right balance between Seebeck coefficient and electrical conductivity of that material, since a low carrier concentration results in a low electrical conductivity of the material but large Seebeck

coefficient.[20,22] In addition, the electronic contribution to the thermal conductivity, κ_{el}, which is generally about $\frac{1}{3}$ of the total thermal conductivity, also increases with carrier concentration.[20]

For the past 20 years, the enhancement of the thermoelectric figure of merit (*ZT*) has been predicted and demonstrated through nanostructural engineering.[12,22-23] Efforts have focused on improving the figure of merit (*ZT*) by reducing lattice thermal conductivity. Three research avenues have been predicted to achieve the increase of *ZT*. One is search for so-called "phonon glass electronic crystals" in which it is proposed that crystal structures containing weakly bound atoms or molecules that "rattle" within an atomic cage should conduct heat like a glass, but conduct electricity like a crystal.[2] Materials attracting attention usually have disorder and complexity within their unit cell, such as skutterudites,[20,22,24] calthrates,[20,22,25] and Zintl phases.[22-23]

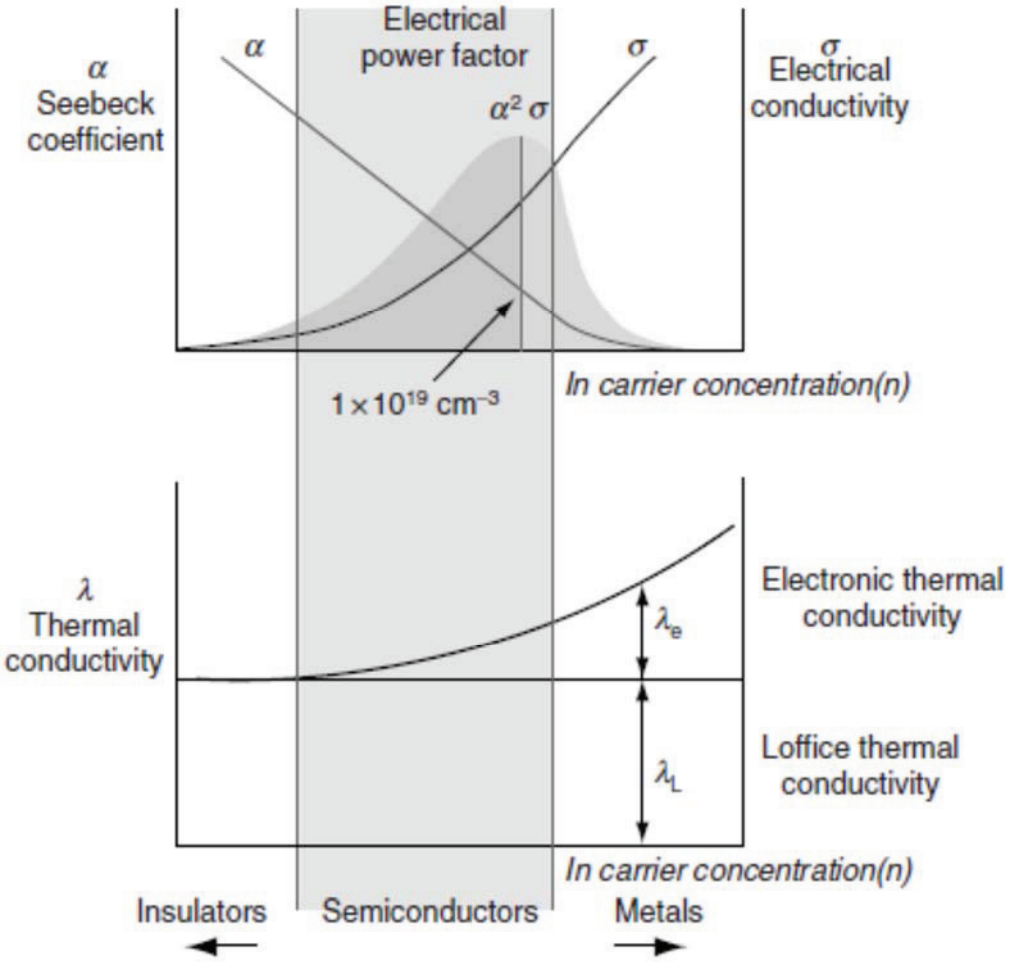

Figure 1.1 Schematic of the dependence of Seebeck coefficient, electrical conductivity, thermal conductivity, and power factor on carrier concentration. Figure reprinted from *CRC Handbook of Thermoelectrics: Macro to Nano* edited by D. M. Rowe. Copyright 2006, Taylor & Francis Group, LLC.

Low-dimensional structures such as quantum wells (materials are so thin as to be considered as two dimensional (2D)), nanowires (small cross-sectional area as to be considered as one dimensional (1D)), and quantum dots (quantum confined in one dimensional (1D)) are selected as the candidates to increase thermoelectric efficiency of nanostructured materials due to the enhancement of phonon scattering introduced by quantum confinement.[13-15,20] The prediction is that the reduced dimensions of these nanostructures will result in an increase in phonon interface scattering and a consequent reduction in lattice thermal conductivity.[20] Recently, nanostructured bulk or nanocomposite materials have become preferred candidates for more scalable applications.[1,21] Randomly distributed nanostructures in nanocomposite materials can lead to a reduction in the lattice thermal conductivity below that of an alloy of the same overall chemical stoichiometry. These materials can be prepared by electrochemically, mechanical alloying or inert-gas condensation methods. Nanometer or micrometer sized particles are then sintered by hot pressing to obtain dense and mechanically nanostrucutured bulk materials.[1,15,21]

1.1.2 Lanthanum Telluride ($La_{3-x}Te_4$)

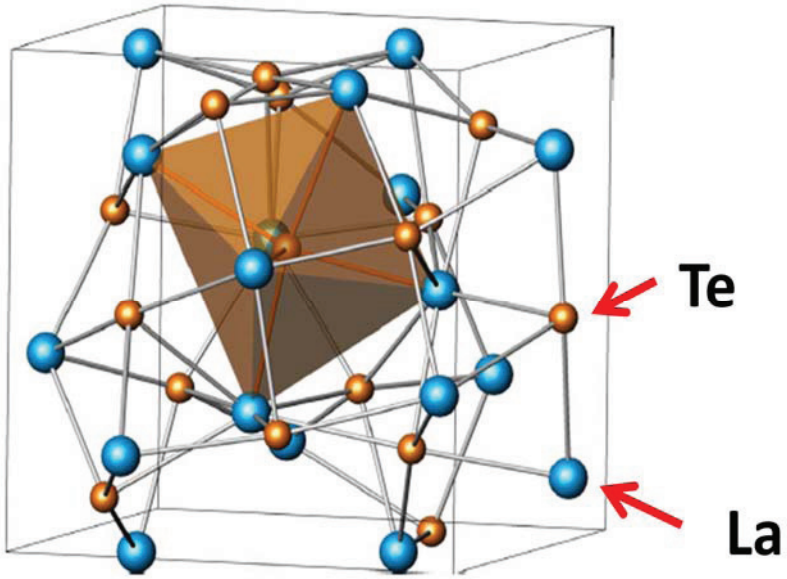

Figure 1.2 The structure of $La_{3-x}Te_4$. Lanthanum atoms are shown in blue and telluride atoms are shown in brown. Figure reprinted from *Phys. Rev. B*, **78** 125205 (2008). Copyright 2008, American Physical Society.

Lanthanum telluride ($La_{3-x}Te_4$) is one of the most efficient n-type thermoelectric materials for high temperature applications. Nanostructured bulk lanthanum telluride by mechanical ball-milling was reported to possess a figure of merit (ZT) greater than 1 at high temperatures near 1300K.[7-8] Lanthanum telluride ($La_{3-x}Te_4$) has a body centered cubic Th_3P_4 defect structure as shown in Figure 1.2. The cubic lattice constant for the $La_{3-x}Te_4$ is 9.628Å and single crystal x-ray diffraction patterns show that its space group is $I\bar{4}3d$, No. 220.[10] Because of the material's unique structure, the vacancies on the rare-earth sites provide disorder and distortion in the lattice, which enhances phonon scattering and then contributes to lower lattice thermal conductivity.[7-8] The presence of

lanthanum vacancies corresponds to x values ranged between 0 and $\frac{1}{3}$. The thermoelectric performance, *ZT*, of lanthanum telluride ($La_{3-x}Te_4$) is enhanced due to the lower lattice thermal conductivity. This enhanced phonon scattering mechanism is reported by Delaire *et al.* and was inferred by measuring the phonon scattering using the wide angular-range chopper spectrometer (ARCS) at the Oak Ridge National Laboratory to get inelastic neutron-scattering spectra in $La_{3-x}Te_4$.[8]

The electronic behavior of $La_{3-x}Te_4$ can be estimated in terms of the composition ratios between lanthanum to tellurium elements.[7-8,26-28] For $0 < x < \frac{1}{3}$, $La_{3-x}Te_4$ behaves like a metal or a heavily doped semiconductor with a higher carrier concentration. When $x = \frac{1}{3}$, each lanthanum donates three electrons to the crystal to become La^{3+} and tellurium takes two electrons to complete its valence band to form Te^{2-}. La_2Te_3 is an ionic solid-structured semiconductor that behaves as an insulator with a much lower carrier concentration. Referring to the phase diagram of Figure 1.3, the compounds of interest need to be in the solid solution composition range between 57 to 60 at.% Te due to the thermoelectric properties of $La_{3-x}Te_4$ changing rapidly with x values since the carrier concentration is proportional to the (1-3x) parameter,[7-8] and controlling the Te to La stioichiometry in lanthanum telluride is thus essential to achieving the optimum thermeoelctric properties of the material.

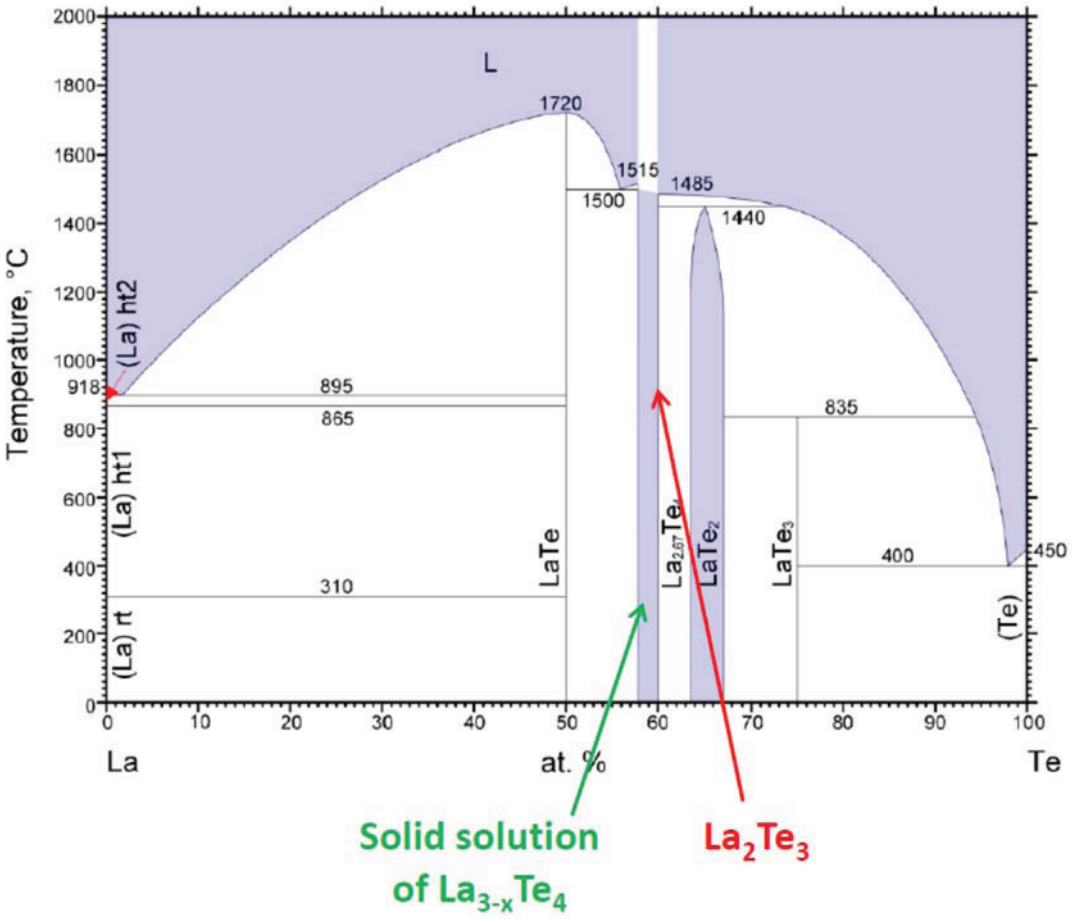

Figure 1.3 Lanthanum-Tellurium phase diagram.[42] The green arrow indicates the solid solution of $La_{3-x}Te_4$ at 57-60 at. % of Te and the red arrow points to the solidus line of La_2Te_3. The phase diagram reprinted from ASM Alloy Phase Diagrams Center. Copyright 2006, ASM International.

1.1.3 Room Temperature Ionic Liquids (RTILs)

A room temperature ionic liquid (RTIL), shown in Figure 1.4(a), is a liquid salt composed solely of anions and cations at room temperature. Shown in Figure 1.4(b), typical solvents used in laboratories such as water, benzene, and methanol are classified as molecular solvents composed of neutral species.[24-26] Room temperature ionic liquids exhibit relatively low viscosity and high conductivity,[17-18,29] and are unreactive towards acids or bases.[30] The liquid salt, which is also non-flammable and non-corrosive, is very safe and laboratory-friendly to work with. Furthermore, room temperature ionic liquids have been shown to be useful for nanoparticle synthesis under vacuum conditions, including electron beam irradiation[31-33] and magnetron sputtering[34-39] onto ionic liquids, due to its low vapor pressure. These are revolutionary findings regarding the feasibility of applying wet chemistry processes in vacuum.

Furthermore, the unique solvent potential of room temperature ionic liquids makes the liquids viable as solutions in which to electrodeposit water-sensitive metals such aluminum and magnesium,[30] reactive elements such as titanium, tantalum, and molybdenum, and semiconductors that are not feasible to electroplate in aqueous electrolytes. The key advantage of using room temperature ionic liquids as the electrolyte for electroplating compared to conventional aqueous solution is that no hydrogen evolution occurs during electrodepositon of the metals.[30,40] In addition, the wide electrochemical potential windows of room temperature ionic liquids can make the electrodeposition of rare-earth elements possible. Therefore, ionic liquids can be used for the fabrication of nanowires using an anodic aluminum oxide (AAO) nanoporous

template-assisted method. Some have even suggested that cation and anion effects from room temperature ionic liquids may influence the morphology and crystal size of deposits.[30,41]

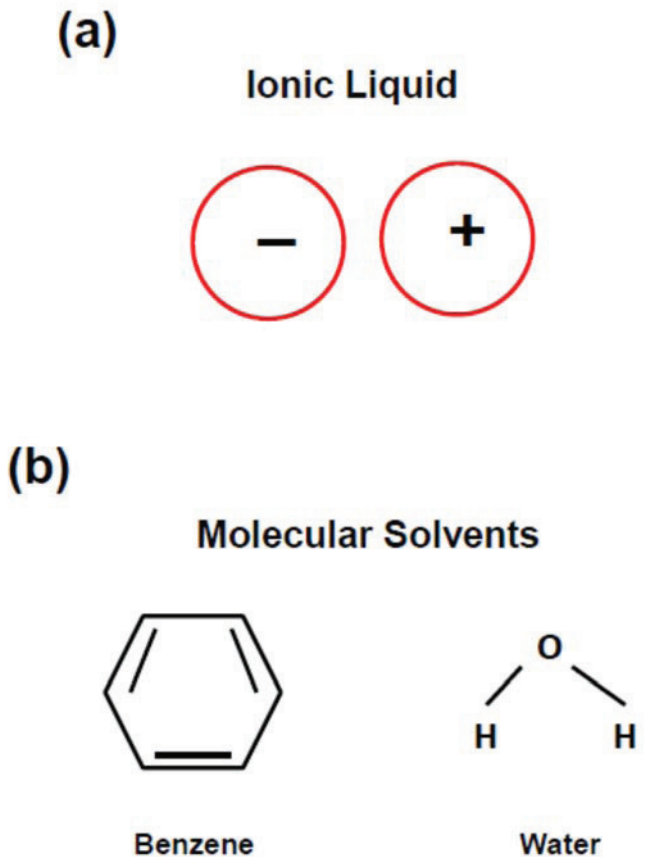

Figure 1.4 (a) Schematic of room temperature ionic liquids composed solely by anions and cations. (b) Schematic of molecular structure of typical molecular solvents such as benzene and water.

1.2 Experimental

This section is an adapted reproduction from *Mater. Res. Soc. Symp. Proc.* Vol. 1543 (2013). Copyright 2013, Materials Research Society.

Tellurium powder (Aldrich Chemistry, 99.8%) was dissolved in concentrated nitric acid to form the oxide cations, $(HTeO_2)^+$, at room temperature until no further reaction occurred. A tellurium seed layer (~100 nm thick) was then electrodeposited onto a nickel or silver substrate (cleaned and etched with HNO_3 : deionized water = 1 : 3) in a three-electrode electrochemical system designed in-house. A nickel or silver substrate served as the working electrode in the experiment. A platinum mesh was used as the counter-electrode and an Ag/AgCl electrode was used as the reference electrode. The electrolyte contained 0.025M $(HTeO_2)^+$ in 3M HNO_3. Potentiastatic deposition was performed at -0.3V vs. Ag/AgCl reference electrode at room temperature.

The ionic liquid, 1-ethyl-3-methylimidazolium bromide (EMIB) (molecular structure is shown in Figure 1.5(b)), was prepared by first stirring 100 ml of 1-methylimidazole (Alfa Aesar, 99%) (molecular structure is shown in Figure 1.5(a)) in a beaker at 70°C followed by slowly adding 300 ml of bromoethane (Sigma-Aldrich, reagent grade, 98%, CH_3CH_2Br) into the beaker. The solution was then allowed to stir about 24 hours at 70°C. Ethyl ether (Fisher Scientific, anhydrous and certified ACS) was added to extract and wash the liquid. The ionic liquid was then stirred at 70°C for 5 hours to burn off any volatiles left in the solution.

(a)

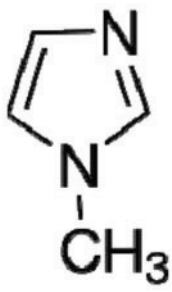

1-methylimidazole

(b)

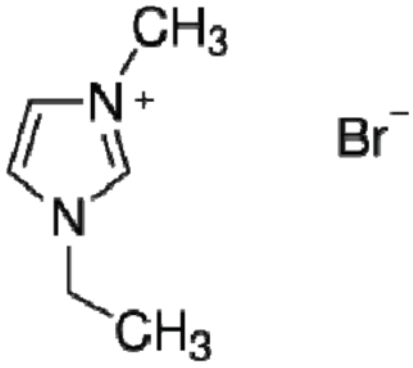

Figure 1.5 Molecular structure of (a) 1-methylimidazole and (b) the anions and cations used as the RTIL solvents in the study.

Lanthanum telluride films were electrodeposited onto the tellurium seed layer in a three-electrode electrochemical system. The nickel or silver substrate served as the working electrode in the experiment. A platinum mesh was used as the counter electrode and an Ag/AgCl electrode was used as the reference electrode. The electrolyte contained 0.9g of lanthanum nitrate hydrate (Aldrich Chemistry, 99.9%) dissolved in 10 ml of 1-ethyl-3-methylimidazolium bromide (EMIB) ionic liquid and a few ml of 0.025M $(HTeO_2)^+$ depending on the La-Te stioichiometric ratio of the desired product as shown in Table 1. The potentiastatic deposition was performed at a range from -1.2 to -1.5V vs. Ag/AgCl reference electrode at room temperature. Ar gas was bubbled into the

electrolyte to remove oxygen from the solution throughout the experiment. A typical deposition duration was about 2 hours and the resulting film thickness was about 1 μm as measured by a profilometer. The deposited films were then rinsed with ethanol and deionized water, followed by storing in vacuum. The morphology of the samples was investigated using a field emission scanning electron microscope (JEOL JSM-6700F) equipped with an energy dispersive x-ray spectrometer (EDAX) for composition analysis. X-ray diffraction patterns of the deposited samples were obtained using a Philips X'Pert X-ray Diffractometer (XRD).

Table 1.1 Electrodeposition Conditions of La and La-Te Alloys.

Counter Electrode	Working Electrode	Electrolyte (in 10 ml ionic liquid)	Deposition Voltage (vs. Ag/AgCl Reference Electrode)	Product
Pt	Ag	0.9g $La(NO_3)_3 \cdot 6H_2O$	-1.5V	La
Pt	Ag	0.2 ml [0.025M $(HTeO_2)^+$] + 0.9g $La(NO_3)_3 \cdot 6H_2O$	-1.5V	LaTe
Pt	Ag	0.3 ml [0.025M $(HTeO_2)^+$] + 0.9g $La(NO_3)_3 \cdot 6H_2O$	-1.5V	$La_{3-x}Te_4$
Pt	Ag	0.2 ml [0.025M $(HTeO_2)^+$] + 0.9g $La(NO_3)_3 \cdot 6H_2O$	-1.2V	La_2Te_3
Pt	Ag	1 ml [0.025M $(HTeO_2)^+$] + 0.9g $La(NO_3)_3 \cdot 6H_2O$	-1.2V	$LaTe_2$
Pt	Ag	0.5 ml [0.025M $(HTeO_2)^+$] + 0.9g $La(NO_3)_3 \cdot 6H_2O$	-1.5V	$LaTe_3$

Table reprinted from *Mater. Res. Soc. Symp. Proc.* Vol. 1543 (2013). Copyright 2013, Materials Research Society.

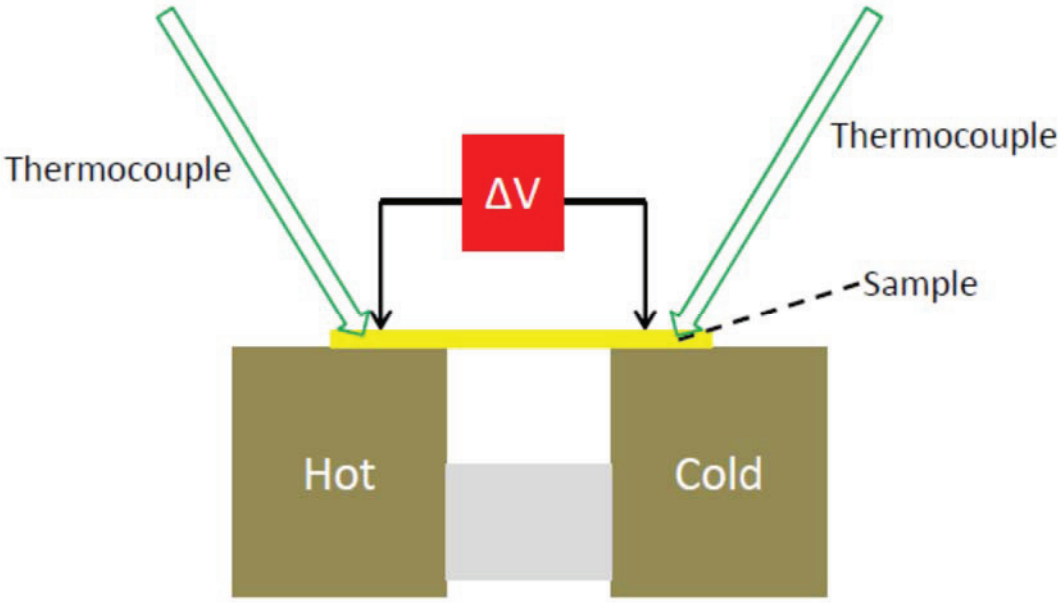

Figure 1.6 Schematic of Seebeck coefficient measurement station.

The measurements of thermoelectric properties were obtained in an isotropic in-plane direction of the films. The Seebeck coefficient was measured by mounting the films on a thermoelectric hot-cold junction pair, with one thermocouple and one voltage measuring probe pressured against the films over each as shown in Figure 1.6. Temperature difference (ΔT) and the difference of thermal energy driven electrical potentials (ΔV) were measured simultaneously using the thermocouples and the voltage measuring probes with a source meter and thermometer. The data were recorded into a computer. The electrical resistance of the electrodeposited films was measured by obtaining *I-V* curves using a two-probe method, and the electrical resistivity of the samples was calculated using $\rho = R\frac{w \cdot t}{l}$, where ρ is the electrical resistivity of the films, R

is the electrical resistance of the films, *w* is the width of the probe tips, *t* is the thickness of the films, and *l* is the distance between the two measuring probes in the measurement.

1.3 Results and Discussion

A tellurium thin film was firstly electrodeposited as the seed layer to minimize the lattice mismatch between the substrate and the deposit to reduce defect formation. The thickness of the lanthanum telluride deposited films was about 1 μm. Since it was essential to synthesize precise stiochiometries of the compound, trials were conducted based on the reduction potentials of each element. The ratio of concentration of each element dissolved in the ionic liquid was varied. The morphologies and chemical compositions of the deposited films were characterized using scanning electron microscopy (SEM), XRD, and EDAX analysis after each deposition. It was critical to determine the correct deposition potentials and solution concentration to control the Te to La ratio.

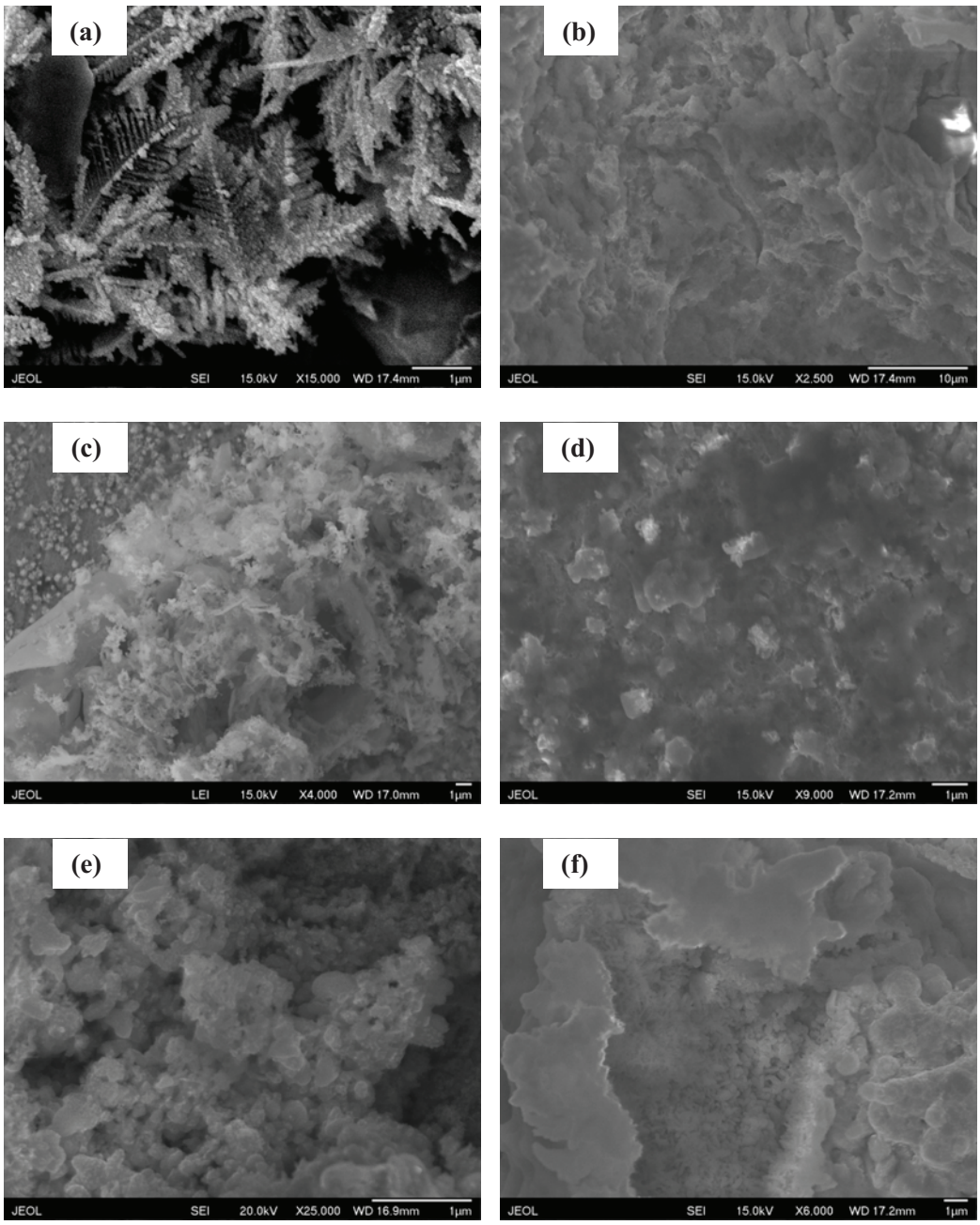

Figure 1.7 Scanning electron microscope images of electrodeposited lanthanum and lanthanum telluride films in 1-ethyl-3-methylimidazolium bromide ionic liquid at different deposition conditions (a) La; (b) LaTe; (c) $La_{3-x}Te_4$; (d) La_2Te_3; (e) $LaTe_2$; (f) $LaTe_3$. Figure reprinted from *Mater. Res. Soc. Symp. Proc.* Vol. 1543 (2013). Copyright 2013, Materials Research Society.

Scanning electron microscope images of electrodeposited films displayed many interesting surface structures as shown in Figure 1.7. Needle-like structures were observed on the electrodeposited La films as shown in Figure 1.7(a). In Figure 1.7(b), the homogenous crystalline LaTe domains with rough surface features covered the entire substrate. On the other hand, it is noted that there were many nanostructured surface features in the $La_{3-x}Te_4$ film as shown in Figure 1.7(c). The nanocrystalline features have many grain boundaries in the microstructure that can scatter phonons more effectively and may result in an enhanced figure of merit (ZT) due to lower thermal conductivity associated with such nanostructured materials.

A typical XRD pattern of the thin film samples is shown in Figure 1.8. Most of the major peaks associated with $La_{3-x}Te_4$ appeared in the pattern. The strong peak around 52° indicates the present of nickel substrate used in the electroplating experiment. The chemical composition of $La_{3-x}Te_4$ films was 41-59 (La-Te) atomic % ratio, as determined from EDAX analysis as shown in Figure 1.9. The strong and sharp peak was identified as corresponding to the silver substrate used in this experiment. The EDAX peaks also indicate the lanthanum and lanthanum telluride samples are free of bulk oxides. The microstructures of La_2Te_3, $LaTe_2$, and $LaTe_3$ were composed of many nanocrystalline granular domains covering the entire substrate as shown in Figure 1.7(d)-(f).

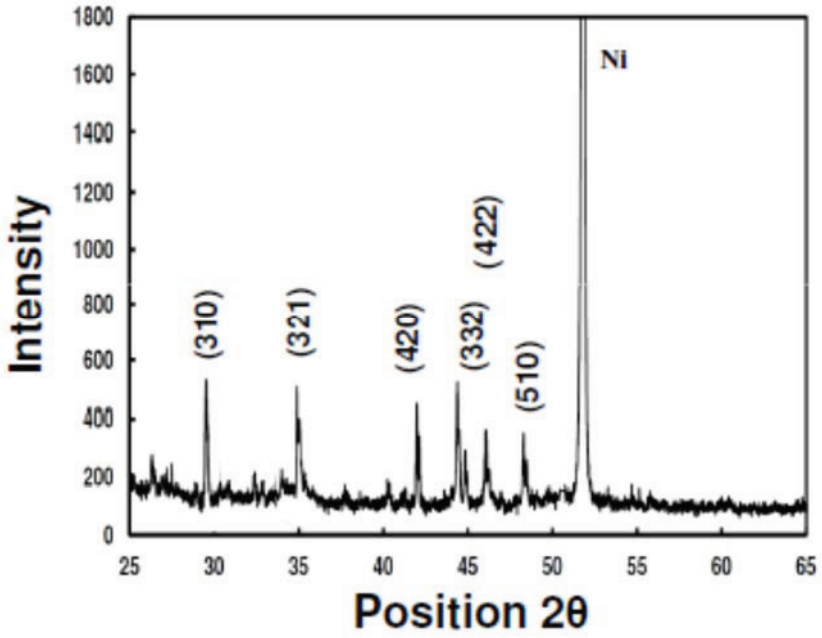

Figure 1.8 X-ray diffraction pattern of electrodeposited $La_{3-x}Te_4$ film on Ni substrate.

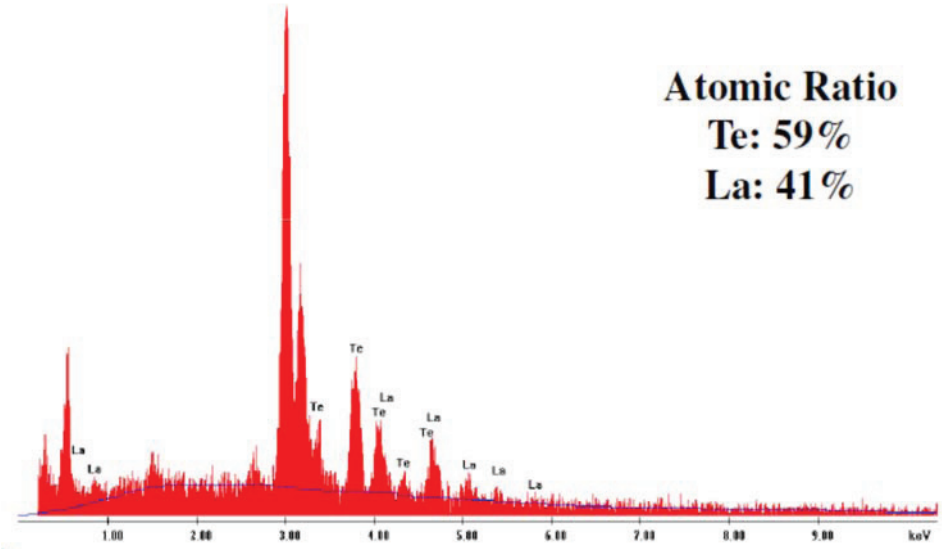

Figure 1.9 EDAX composition analysis of electrodeposited $La_{3-x}Te_4$ film on Ag substrate. Figure reprinted from *Mater. Res. Soc. Symp. Proc.* Vol. 1543 (2013). Copyright 2013, Materials Research Society.

Table 1.2 Measured Room Temperature Thermoelectric Prosperities.

Sample	La at.%	Te at.%	S (μV/K)	ρ (mΩ-cm)	P (W/mK^2)
$La_{2.82}Te_4$	42.4	57.6	-51	3.2	8.1×10^{-5}
$La_{2.72}Te_4$	40.9	59.1	-173	10.5	28.5×10^{-5}

Table 1.2 shows the room temperature Seebeck coefficients and electrical resistivity measured in house. The measured Seebeck coefficients and electrical resistivity of our deposited thin films are very similar to thermoelectric properties of the state-of-the-art bulk samples synthesized by mechanical alloying and hot-press sintering and the measurements are within the standard deviations reported by May *et al.*[7-8] The calculated power factor of the deposited films ranges from 8.1×10^{-5} to 28.5×10^{-5} (W m^{-1} K^{-2}). We do not report the room temperature thermal conductivities of the electrodeposited samples because of the difficulty in making such measurements on thin films, since parasitic surface effects can strongly influence the measurements strongly due to the smaller dimensions and large aspect ratios characteristic of the samples.[20] Furthermore, the electrodeposited $La_{3-x}Te_4$ thin film as shown in Figure 1.7(c) shows rough and anisotropic surface features, which will contribute to large differences between cross-plane and in-plane thermal conductivity measurements. It will be necessary to improve the surface quality and morphologies of the thin films in order to obtain good measurements by, for example, adding grain refiners in the electrolyte, optimizing the reduction potentials for the electroplating, and by electroplating lanthanum telluride thin films in a controlled inert gas environment.

1.4 Conclusions

The feasibility of electrodepositing pure lanthanum and lanthanum telluride compounds in ambient conditions has been demonstrated. Scanning electron microscope images show that surface morphologies of the deposited films varied from needle-like to granular structures depending on the deposition conditions. Such nanostructured surface features on the electrodeposited samples may be responsible for enhancing ZT because high density of grain boundaries may scatter phonons more effectively resulting in a lowering of the thermal conductivity. The measured Seebeck coefficients and electrical resistivity of the electrodeposited thin films are close to the state-of-the-art thermoelectric properties of bulk samples synthesized by mechanical alloying and the hot-press sintering. The calculated power factor of the deposited films ranged from 8.1 x 10^{-5} to 28.5 x 10^{-5} (W m^{-1} K^{-2}). X-ray diffraction (XRD) patterns and the energy dispersive x-ray (EDAX) composition analysis of electrodeposited $La_{3-x}Te_4$ films indicated that the samples were single phase materials.

1.5 Future Work

Given the promising behavior observed in this work, clearly the next step is to produce materials for which thermal conductivity can be measured so that the value of ZT can be obtained. The reproducibility of electrodeposited lanthanum telluride thin films can be improved by synthesizing the material in a well-controlled inert gas environment such as a glove box to prevent possible oxide formation during the fabrication process. In addition, the electrodeposition parameters such as precise

reduction potential and concentration of deposit in electrolyte can be optimized. It is also worth noting that the detail of mechanism of metal and alloy electrodeposition in ionic liquid should be examined. It is also proposed that the reported electroplating technique could be used to synthesize elemental lanthanum and lanthanum telluride nanowire arrays by using conventional template methods with anodic aluminum oxide (AAO) nanoporous membranes. These samples could be studied to investigate the prediction that such reduced dimensional materials will display even lower lattice thermal conductivity due to enhancement of phonon interface scattering introduced by quantum confinement.

Bibliography

1. J. W. Swart, editor, *Solid State Circuits Technologies*, ISBN 978-953-307-045-2, pp. 462, INTECH, Croatia (2010).
   URL: http://www.intechopen.com/download/get/type/pdfs/id/6497
2. A. K. Samal and T. Pradeep, Lanthanum Telluride Nanowires: Formation, Doping, and Raman Studies, *J. Phys. Chem. C.* **114**, 5871-5878 (2010).
3. J. C. Kopera, "Inside the Nickel Metal Hydride Battery," Cobasys (2004).
   URL: http://www.cobasys.com/pdf/tutorial/inside_nimh_battery_technology.pdf
4. S. Gorman, As hybrid cars gobble rare metals, shortage looms, © Thomson Reuters 2011, Aug 31, 2009. URL: http://www.reuters.com/article/2009/08/31/us-mining-toyota-idUSTRE57U02B20090831
5. P. Bäuerlein, C. Antonius, Jens Lőffler, and Jőrg Kűmpers, Progress in high-power nickel-metal hydride batteries, *J. of Power Sources*. **176**, 547-554 (2008).
6. "Lanthanum," Chemicool Periodic Table, Chmicool.com, Oct. 17, 2012.
   URL http://www.chemicool.com/elements/lanthanum.html.
7. A. May, J.-P. Fleurial, and G. J. Snyder, Thermoelectric performance of lanthanum telluride produced via mechanical alloying, *Phys. Rev. B* **78**, 125205 (2008).
8. O. Delaire, A. F. May, M. A. McGuire, W. D. Porter, M. S. Lucas, M. B. Stone, D. L. Abernathy, V. A. Ravi, S. A. Firdosy, and G. J. Snyder, Phonon density of states and heat capacity of $La_{3-x}Te_4$, *Phys. Rev. B* **80**, 184302 (2009).

9. G. D. Badge, S. D. Sartale, and C. D. Lokhande, Spray pyrolysis deposition of lanthanum telluride thin films and their characterizations, *Mate. Chem. and Phys*. **89**, 402-405 (2005).
10. T. H. Ramsey, H. Steinfink, and E. J. Weiss, The Phase Equilibria and Crystal Chemistry of the Rare Earth-Group VI Systems. IV. Lanthanum-Tellurium, *Inorg. Chem.*, **4**(8), 1154-1157 (1965).
11. T. H. Ramsey, H. Steinfink, and E. J. Weiss, Some Thermoelectric Properties of Polycrystalline Lanthanum Telluride, LaTe1.7 to LaTe2.0, *J. Appl. Phys*. **34**, 2917 (1963).
12. G. Chen, M. S. Dresselhaus, G. Dresselhaus. J. P. Fleurial, and T. Caillat, Recent development in thermoelectric materials. *Int. Mater. Rev.* **48**, 45-66 (2003).
13. L. D. Hicks and M. S. Dresselhaus, Effect of quantum-well structures on the thermoelectric figure of merit, *Phys. Rev. B* **47**, 12727 (1993).
14. L. D. Hicks and M. S. Dresselhaus, Thermoelectric figure of merit of a one-directional conductor, *Phys. Rev. B* **47**, 16631 (1993).
15. M. S. Dresselhaus, G. Chen, M. Y. Tang, R. G. Yang, H. Lee, D. Z. Wang, Z. F. Ren, J.-P. Fleurial, and P. Gogna, New directions for low-dimensional thermoelectric materials, *Adv. Mater.* **19** (2007).
16. J.-P. Fleurial, A. Borshchevsky, M. A. Ryan, W. Phillips, E. Kolawa, T. Kacisch, and R. Ewell, Proceedings of XVI International Conference on Thermoelectrics, Dresden, Germany, p. 641, 1997.
17. M. J. Earle and K. R. Sedden, Ionic liquids: Green solvents for the future, *Pure Appl. Chem.* **72** (7), 1391-1398 (2000).

18. Covalent Associates, Inc., *Introduction to Ionic Liquids*. URL:http://www.covalentassociates.com/Introduction%20to%20Ionic%20Liquids.pdf
19. D. M. Rowe, editor, *CRC Handbook of Thermoelectrics*, CRC Press, Boca Raton, FL (1995).
20. D. M. Rowe, editor, *CRC Handbook of Thermoelectric: Macro to Nano,* CRC Press, Taylor & Francis Group, LLC, Boca Raton, FL (2006).
21. J. P. Fleurial, Thermoelectric power generation materials: technology and application opportunities, *JOM* Vol. **16** issue 4: 79-85 (2009).
22. G. J. Snyder and E. S. Toberer, Complex Thermoelectric Materials, *Nature Materials* **7**, 105-114 (2008).
23. S. M. Kauzlarich, S. R. Brown, and G. J. Snyder, Zintl Phases for thermoelectric devices, *Dalton Trans.* 2099-2107 (2007).
24. C. Uher, in *Thermoelectric Materials Research I* (ed. T. Tritt). 139-253, Semiconductors and Semimetals Series **69**, Elsevier (2001).
25. G. S. Nolas, J. Poon, and M. Kanatzids, Recent developments in bulk thermoelectric materials, *Mater. Res. Soc. Bull.* **31**, 199-205 (2006).
26. M. Cutler, J. Leavy, and R. Fitzpatrick, Electron transport in semimetallic cerium sulfide, *Phys. Rev.* **133**, A1143 (1964).
27. M. Cutler and J. Leavy, Electron transport in high-resistivity cerium sulfide, *Phys. Rev.* **133,** A1153 (1964).
28. T. H. Ramsey, H. Steinfink, and E. J. Weiss, Thermoelectric and Electrical Measurements in the La-Te System, *J. Appl. Phys.* **36** (2), 548-553 (1965).

29. T. Tsuda, C. L. Hussey, and G. R. Stafford, Progress in Surface Finishing with Lewis Acidic Room-Temperature Chloroaluminate Ionic Liquids, *ECS Trans.* **3** (35), 217-231 (2007).

30. M. Armand, F. Endres, D. R. MacFarlane, H. Ohno, and B. Scrosati, Ionic-liquid materials for the electrochemical challenges of future, *Nature Materials* **8**, 621-629 (2009).

31. A. Imanishi, M. Tamura, and S. Kuwabata, Formation of Au nanoparticles in an ionic liquid by electron beam irradiation, *Chem. Commun.* **13**, 1775-1777 (2009).

32. T. Tsuda, S. Seino, and S. Kuwabata, Gold nanoparticles prepared with a room-temperature ionic liquid-radiation irradiation method, *Chem. Commun.* **44**, 6792-6794 (2009a).

33. T. Tsuda, T. Sakamoto, T. Nose, S. Seino, A. Imanishi, T. Uematsu, and S. Kuwabata, Irradiation-Induced Metal Nanoparticles in Room-Temperature Ionic Liquid, *ECS Trans.* **33** (7), 543-554 (2010a).

34. Y. Hatakeyama, M. Okamoto, T. Torimoto, S. Kuwabata, and K. Nishikawa, Small-Angle X-ray Scattering Study of Au Nanoparticles Dispersed in the Ionic Liquids 1-Alkyl-3-methyllmidazolium Tetrafluoroborate, *J. Phys. Chem. C* **113**, 3917-3922 (2009).

35. Y. Hatakeyama, S. Takahashi, and K. Nishikawa, Can Temperature Control the Size of Au Nanoparticles Prepared in Ionic Liquids by the Sputter Deposition Technique?, *J. Phys. Chem. C* **114**, 11098-11102 (2010).

36. T. Kameyama, Y. Ohno, T. Kurimoto, K. Okazaki, T. Uematsu, and T. Torimoto, Size control and immobilization of gold nanoparticles stabilized in an ionic liquid

on glass substrates for plasmonic applications, *Phys. Chem. Chem. Phys.* **12**, 1804-1811 (2010).

37. T. Suzuki, K. Okazaki, T. Kiyama, S. Kuwabata, and T. Torimoto, A Facile Synthesis of AuAg Alloy Nanoparticles Using a Chemical Reaction Induced by Sputter Deposition of Metal onto Ionic Liquids, *Electrochemistry* **77**, 636-638 (2009).
38. T. Tsuda and C. L. Hussey, Electrochemistry of room temperature ionic liquids and melts, R. E. White (ed.) *Modern Aspects of Electrochemistry* Vol. **45**, Springer Science + Business Media, New York, pp. 63-174 (2009).
39. T. Tsuda, K. Yoshii, T. Torimoto, and S. Kuwabata, Oxygen reducation catalytic ability of platinum nanoparticles prepared by room-temperature ionic liquid-sputtering method, *J. Power Sources* **195**, 5980-5985 (2010b).
40. S. Legeai*,* S. Diliberto, N. Stein, C. Boulanger, J. Estager, N. Papaiconomou, and M. Draye, Room-temperature ionic liquid fro lanthanum electrodepsoition, *Elec. Comm.* **10**, 1661-1664 (2008).
41. A. P. Abbott and K. J. McKenzie, Application of ionic liquids to the electrodeposition of metals, *Phys. Chem. Chem. Phys.* **8**, 4265-4279 (2006).
42. H. Okamoto, La-Te (Lanthanum-Tellurium), Binary Alloy Phase Diagrams, II Ed., Ed. T. B. Massalski, Vol.3, 1990, p 2430-2431. ASM Alloy Phase Diagrams Center, P. Villars, editor-in-chief; H. Okamoto and K. Cenzual, section editors; ASM International, Materials Park, OH, USA, 2006-2013.

    URL: http://www1.asminternational.org/asmenterprise/APD/PrintViewAPD.aspx

Chapter 2

Synthesis and Characterization of Vertically-Aligned Gold Nanowire Arrays Ferromagnetic Composite Films

2.1 Introduction

Ordered nanocomposite structures have attracted significant interest as their unique electrical and optical properties can lead to localized surface plasmon resonance (LSPR). This behavior has to potential to improve current commercial lab-on-a-chip surface enhanced Raman scattering (SERS) technologies such as portable Raman systems, used to detect and identify chemical and biological agents and explosive compounds at trace levels.[1] LSPR describes a resonance phenomenon of surface electron density in metallic nanoscale structures where the characteristic length scale of the material is smaller than the wavelength of incident light.[2] LSPR signaling enhancement depends on the type of the material (gold, silver, and platinum), and the size, shape, and spacing of nanostructured materials.[3-6] For gold, LSPR leads to strong plasmon absorption in the visible wavelength regime.[3] Highly ordered gold nanowire arrays can sustain large electromagnetic fields at a high density of sites within the structure upon the

excitation of light.[4-6] This structure becomes an excellent substrate for LSPR enhancement.

However, other than gold, silver, and platinum, there are still many classes of materials that have plasmon resonance and other interesting optical-electronic properties. It has been known that ferromagnetic materials such as nickel or cobalt having a spectral position of the plasmon resonance similar to that of silver.[6] Therefore, the combination of the ferromagnetic resonance with plasmonic resonance may lead to a novel material for LSPR signaling enhancement.[6-7] Here we report on the fabrication and characterization of vertically-aligned gold nanowire arrays in ferromagnetic matrices (nickel and iron). It is thought that the magnetic response of the ferromagnetic matrices may couple with the plasmonic behavior, thus amplifying the LSPR response. Our goal in this work is to synthesize large area, reproducible, and homogeneous substrates that may have applications as LSPR materials for biological and chemical sensors.

2.1.1 Localized Surface Plasmon Resonance (LSPR)

The free electrons in noble metals are free to travel through the material. The mean free path due to phonon scattering in bulk gold and silver is ~ 50 nm. In nanostructured materials smaller than this mean free path, the electron scattering is expected to be dominated by scattering at the surfaces.[8] Localized surface plasmon resonance (LSPR) describes a induced resonance phenomenon of surface free electron waves in noble metallic nanostructures such as nanoparticles, nanoscale rough surface, and nanowires, where the characteristic length scale of the materials is smaller than the wavelength of incident light.[2,9-10] This resonance is a coherent collective oscillation of the

surface electrons in the conduction band excited and polarized by the incident light (electromagnetic wave).[5,7] As shown in Figure 2.1, an incident light interacts with nanoparticles that are much smaller in size than the wavelength of that incident light. This condition leads to a plasmon that oscillates locally around the particles (localized surface plasmon resonance) with a frequency which matches the frequency of the incident light. The resonance causes a collective oscillation of the conduction electrons in the metal nanoparticles.[11]

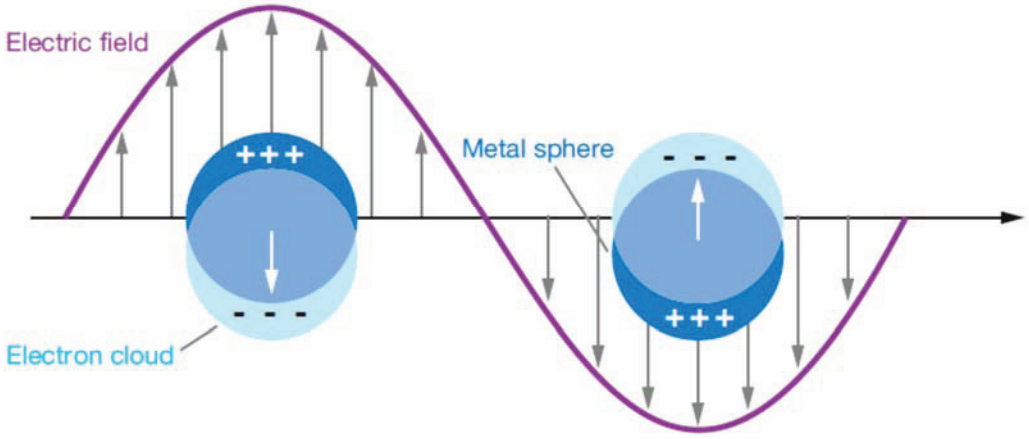

Figure 2.1 Schematic of a localized surface plasmon for a sphere, showing the displacement of the conduction electron charge could relative to the nuclei. Figure reprinted from *Annu. Rev. Phys. Chem.* **58**, 267-297 (2007). Copyright 2007, Annual Reviews.

Since the LSPR occurs at the surface, as the size or the shape of the nanoparticles change, the surface geometry also changes, resulting in a shift in the electromagnetic field on the surface. This causes a change in the frequency of collective oscillation of the conduction electrons, generating different cross-sections for LSPR respondence.[15] Furthermore, if the dielectric constant of the surrounding material of the nanoparticles changes, this will have an effect on the oscillation frequency of the surface electrons due

to the varying ability of the surface to accommodate electron charge density from the nanoparticles.[12] Therefore, the frequency and intensity of LSPR highly depend on the type of the material (gold, silver, or platinum), the size, the shape, the interspacing, and the dielectric constant of nanoparticles and their surrounding materials.[3-6,8,11-13]

Based on the development of modern methods extending from the Mie solution to Maxwell's equations describing the surface plasmon resonance for a small sphere interacting with an electromagnetic field which can be used to calculate the surface plasmon resonance for arbitrary geometries.[12] Gold nanorods (nanowires) have generated interest as materials to study LSPR because an increase in the aspect ratio of gold nanorods contributes to the enhancement of the intensity and the longitudinal plasmon resonance, resulting in an enhancement of the electromagnetic field.[12,14] Therefore, highly ordered gold nanowire arrays can sustain larger electromagnetic fields at a high density of sites within the structure upon the excitation and polarization of incident light.[4-6] As a result, vertically-aligned gold nanowire arrays may prove to be excellent substrates for LSPR enhancement.

Nobel metals such as gold, silver, or platinum are common materials for determining LSPR effect because their energy levels of d-d transitions exhibited LSPR are in the visible range of the spectrum.[8,12] As a result, the wavelengths of the incident light that cause this collective oscillation conduction electrons are selectively absorbed by nanostructured materials and can be measured using ultraviolet-visible (UV-Vis) spectropscopy.[5,11] Also, the formation of enhanced electromagnetic fields that extend from the metal nanostructured surfaces is responsible for the enhancement observed in surface-enhanced Raman scattering (SERS).[7,9,11] Therefore, not only is LSPR a powerful

technique for chemical and biological sensing, but also is responsible for the electromagnetic field enhancements that leads to surface-enhanced Raman scattering (SERS).[7,9] With the some understandings of LSPR effect, the purpose of this work is to develop a synthesis method for large area, reproducible, and homogeneous samples that may have applications for localized surface plasmon resonance effects.

2.2 Experimental

Vertically-aligned gold nanowires grown on a gold substrate were fabricated by electrodeposition. Anodic aluminum oxide (AAO) nanoporous membranes (Whatman, porosity: 40%, pore spacing: ~ 140 nm, membrane thickness: ~ 60 μm) which were about 60 μm thick and had pore size about 100 nm were used as templates in these experiments. A gold film about 1 μm thick was electron beam evaporated onto the back side of the AAO membrane and served as the working electrode. A platinum mesh was used as the counter electrode and an Ag/AgCl electrode was used as the reference electrode in the three-electrode electrochemical system designed in house. The electrolyte was gold plating solution (Alfa Aesar, electroless, metal content ≈ 3.7 g/L). Potentiastatic deposition was run at -1 V vs. Ag/AgCl reference electrode at room temperature for 1 hour. Gold ions in the electrolyte are restricted to only be reduced into elemental gold inside the nanopores. The AAO template was then dissolved in a 4 M aqueous sodium hydroxide (NaOH) solution at room temperature for 2 hours. The exposed gold nanowires on the substrate were subsequently thoroughly rinsed with DI water.

Vertically standing gold micropilliars grown on a gold substrate were fabricated by a similar electrodeposition process as described above. Polycarbonate membranes

(Whatman®) which are about 12 μm thick and have pore size about 5 μm were used as templates in these experiments. A copper film about 1 μm thick was electron beam evaporated onto the back side of the AAO membrane and served as the working electrode. A platinum mesh was used as the counter electrode and an Ag/AgCl electrode was used as the reference electrode in the three-electrode electrochemical system designed in house. The electrolyte was gold plating solution (Alfa Aesar, electroless, metal content ≈ 3.7 g/L). Potentiastatic deposition was run at -1 V vs. Ag/AgCl reference electrode at room temperature for 15 minutes. Gold ions in the electrolyte were restricted to only being reduced into elemental gold inside the micropores. The polycarbonate template was dissolved in dichloromethane (Sigma-Aldrich, anhydrous, ≥ 99.8%) at room temperature for 30 minutes and then the sample was ultrasonicated in the suspension for 5 minutes. The gold microwires with the substrate were thoroughly rinsed with deionized water.

After etching away the AAO nanoporous membrane, nickel was electron beam evaporated at a deposition rate of approximately 1 Å/s onto the exposed gold nanowires resulting in a nanocomposite composed of a nickel matrix with embedded gold nanowires. Another set of nickel matrix nanocomposites were synthesized by electrodepositing the nickel onto the gold nanowires using the same three-electrode electrochemical system discussed previously. The electrodeposition was carried out at a constant current density of 1 mA/cm^2 at room temperature for 2 hours. The counter electrode and reference electrode used in the experiment were nickel foils (Alfa Aesar, 99.95%, 0.25 mm thick). The electrolyte used in the electrochemical process was a 1.24 M nickel sulfate hexahydrate (Sigma Aldrich, ACS reagent, 99%, 227676-500G), 0.5 M

boric acid (Alfa Aesar, 99.99%, metal basis, CAS#10043-35-3), 0.02 M $NiCl_2$ (Sigma Aldrich, 98%, 339350-250G), 0.5 g/L sodium dodecyl sulfate (SDS) (Sigma Aldrich, for molecular biology, L4390-100G), and 0.1 g/L coumarin 6 (Sigma Aldrich, 98%, 442631-5G) aqueous solution.

Samples with iron matrices were fabricated by electrodepositing the iron onto the gold nanowires from an aqueous solution of 1 M iron sulfate hephahydrate (Sigma Alrich, plant cell culture tested, ≥ 99%), 0.43 M H_4ClN (Sigma Aldrich, for molecular biology, ≥ 99.5%, A9434-500G), 0.3 M NaCl (Sigma Aldrich, BioXtra, ≥ 99.5%, S7653-1KG), 15 g/L L-asccorbic acid (Alfa Aesar, 99+%, CAS#50-81-7), 1 g/L saccharin (Sigma Aldrich, 98+%, 109185-500G) and 1 g/L sodium dodecyl sulfate (SDS) (Sigma Aldrich, for molecular biology, L4390-100G). The electrochemical deposition was carried out for 2 hours at a constant current density of 1.5 mA/cm^2 at room temperature. A platinum mesh was used as the counter electrode and an Ag/AgCl electrode as the reference electrode. The morphology of the samples was investigated using a JEOL JSM-6700F field emission scanning electron microscope (SEM). The chemical composition of the deposited films was characterized using energy dispersive x-ray (EDAX) analysis.

2.3 Results and Discussion

The anodic aluminum oxide (AAO) nanoporous membrane as shown in Figure 2.2 used in this work exhibited a hexagonally arranged nanoporous arrays with pore diameter and pore interspacing distance about 100 nm and 150 nm, respectively. Figure 2.3(a) and 2.2(b) show the top view and the side view, respectively of the scanning

electron micrographs of vertically-aligned gold nanowire arrays on a gold substrate after dissolution of the AAO template. It can be seen that the nanowire arrays were highly dense and well attached to the gold substrate. The average diameter of gold nanowires was about 100 nm, which is consistent with the pore size of the AAO template used in the electrochemical deposition. The nanowires have initial lengths of approximately 500 to 800 nm, corresponding to an aspect ratio of 5 to 8. Figure 2.4 show the vertically standing Au micropillars grown on an Au substrate. These pillars are strongly attached to the Au substrate.

Figure 2.5(a) shows the SEM image of vertically-aligned gold nanowires (white dots) embedded in nickel matrices (light gray areas) manufactured by electron beam evaporating nickel onto the electrodeposited nanowire array. The interspacing of the exposed gold nanowires ranged from a few hundreds of nanometers to a few micrometers. Figure 2.5(b) shows the SEM image of vertically-aligned gold nanowires (white dots) embedded in nickel matrices (light gray areas) manufactured by electrodepositing nickel around the gold nanowire array. Comparing between Figure 2.5(a) to Figure 2.5(b), it is seen that the electrodeposition technique preserved the spacing of the exposed gold nanowires better than the electron beam evaporation technique did. In addition, the surface of the nickel matrix by electron beam evaporation was rougher than that obtained by electrodeposition. Energy dispersive x-ray analysis gave a composition of 98 atomic % of gold at the tips of the exposed gold nanowires indicating minimal coating of the nickel by both electron beam evaporation and electrodeposition. Figure 2.6 shows the SEM image of vertically-aligned gold nanowires (white dots) embedded in iron matrices (gray areas) manufactured by electrodeposition of

iron onto the gold nanowire array. The spacing of the exposed gold nanowires ranged from a few hundreds of nanometers to a few micrometers. For both techniques, the density of gold nanowires across the nickel and iron matrices was homogenous regardless of the fabrication parameters.

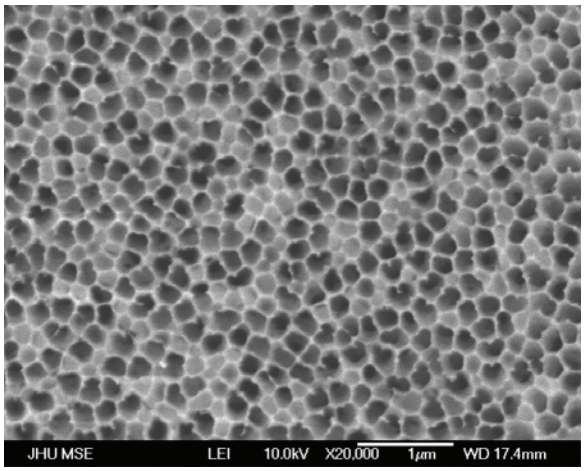

Figure 2.2 Scanning Electron Microscope image of top view of the nanoporous anodic aluminum oxide (AAO) membrane.

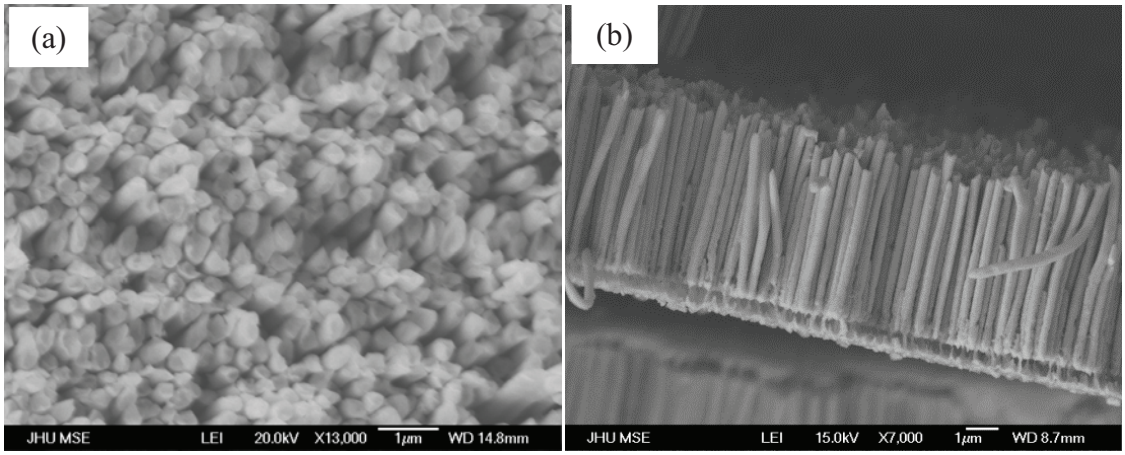

Figure 2.3 Scanning Electron Microscope images of (a) vertically-aligned gold nanowires on a gold substrate, (b) cross-sectional view of vertically-aligned gold nanowires on a gold substrate. The wire diameter is about 100 nm.

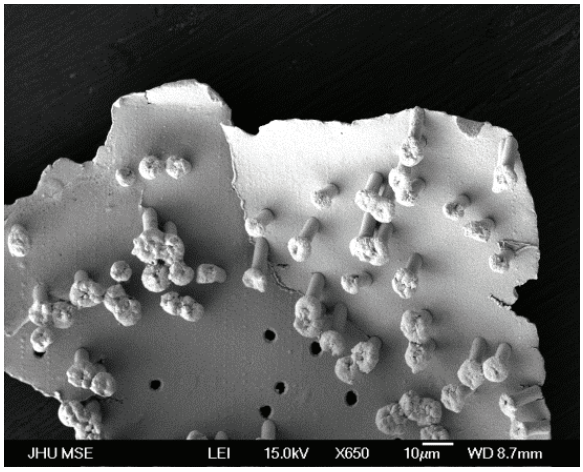

Figure 2.4 Scanning Electron Microscope image of top down view of vertically-aligned gold micropillars on a gold substrate. The wire diameter is about 5 μm.

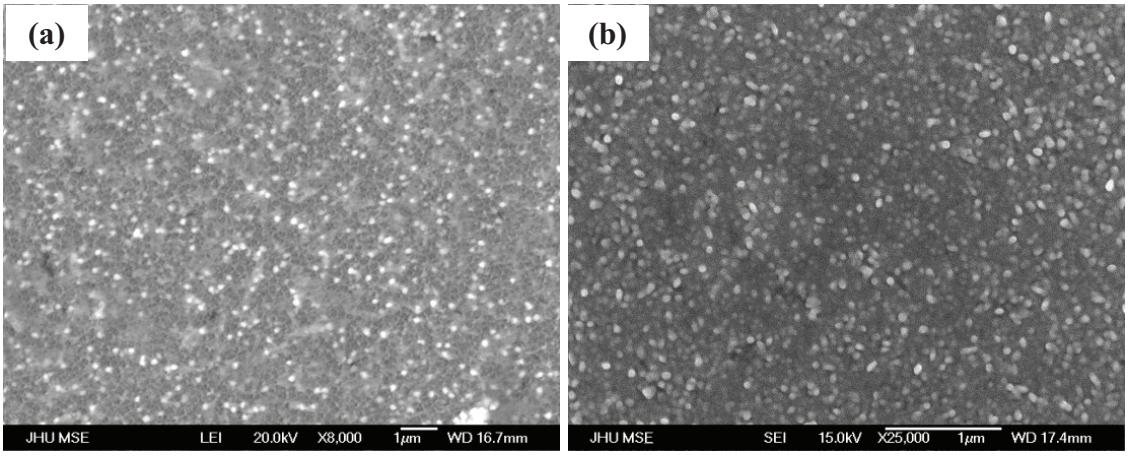

Figure 2.5 Scanning Electron Microscope image of the top down view of vertically-aligned elemental gold nanowires embedded in nickel matrices using (a) electron beam evaporation and; (b) electrodeposition.

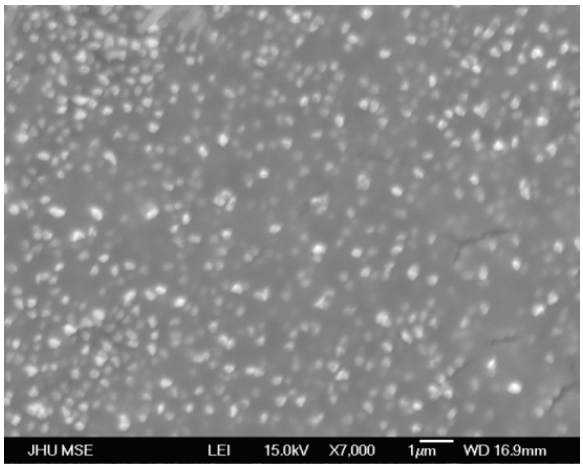

Figure 2.6 Scanning Electron Microscope image of the top down view of vertically-aligned elemental gold nanowires embedded in iron matrices using electrodeposition.

2.4 Conclusions

Vertically-aligned gold nanowires onto a gold substrate were fabricated by electrodeposition through commercially available anodic aluminum oxide (AAO) nanoporous membranes with a constant potential -1 V vs. Ag/AgCl reference electrode at room temperature. Scanning electron microscopy images show that the gold nanowire arrays were highly dense and strongly attached to the gold substrate after dissolution of the template. Nanocomposites composed of gold nanowire arrays embedded in ferromagnetic matrices were synthesized by evaporation or electrodeposition the ferromagnetic materials onto the gold nanowires. This is the first time such ferromagnetic matrix-second phase gold nanowire nanocomposite thin films have been synthesized. The electrodeposition technique preserved the spacing of the exposed gold nanowires better than the electron beam evaporation technique dis. For both techniques, the density of gold nanowires across the nickel and iron matrices was homogenous regardless of the fabrication parameters.

2.5 Future Work

Now that we have shown that nanocomposite iron matrix-gold nanowires can be produced, samples should be fabricated for which localized surface plasmon resonance measurement can be made to see if these materials display the predicted enhancement of LSPR. Furthermore, the coercivities of the nanocomposite films should be characterized. This effectively measures the residual magnetization in the samples following the removal of an externally applied field. The coercivity measurements would indicate if the samples can maintain a reasonable magnetization for a period of time. If so, any LSPR enhancement could be measured when the nanocomposite film is polarized in a large magnetic field to determine the influence upon the response. The magnetic field component would act in addition (depending upon its orientation) to the plasmonic field, thus amplifying the LSPR response.

Bibliography

1. P. Daniel, NRL Scientists Elevate Warfighter Readiness against Invisible Threats (2011).

   URL: http://www.nrl.navy.mil/media/news-releases/2011/nrl-scientists-elevate-warfighter-readiness-against-invisible-threats

2. K. Mitsui, Y. Handa, and K. Kajikawa, Optical fiber affinity biosensor based on localized surface plasmon resonance, *Appl. Phys. Lett.* **85**, 4231 (2004).

3. C. J. Murphy, A. M. Gole, S. E. Hunyadi, and C. J. Orendoff, One-Dimensional Colloidal Gold and Silver Nanostructures, *Inorg. Chem.* **45**, 7544-7554 (2006).

4. L. Billot, M. L. de la Chapelle, A. S. Grimault, A. Vial, D. Barchiesi, J.-L. Bijeon, P.-M. Adam, and P. Royer, Surface enhanced Raman scattering on gold nanowire arrays: evidence of strong multipolar surface plasmon resonance enhancement, *Chem. Phys. Lett.* **422**, 303-307 (2006).

5. H. M. Hiep *et al.,* A Localized surface plasmon resonance based immunosensor for the detection of casein in milk, *Sci. Technol. Adv. Mater.* **8** (4), 331-338 (2007).

6. G. Sauer, G. Brehm, S. Schneider, H. Graener, G. Seifert, K. Nielsch, J. Choi, P. Göring, U. Gösele, P. Miclea, and R. B. Wehrspohn, Surface-enhanced Raman spectroscopy employing monodisperse nickel nanowire arrays, *Appl. Phys. Lett.* **88**, 023106 (2006).

7. K. A. Willets and R. P. Van Duyne, Localized Surface Plasmon Resonance Spectroscopy and Sensing, *Annu. Rev. Phys. Chem.* **58**, 267-297 (2007).

8. E. Petryayeva and U. Krull, Localized surface plasmon resonance: Nanostructures, bioassays and biosensing – A review, *Analytica Chimica Acta* **706**, 8-24 (2011).
9. A. J. Haes, S. Zou, G. C. Schatz, and R. P. Van Duyne, A Nanoscale Optical Biosensor: The Long Range Distance Dependence of the Localized Surface Plasma Resonance of Noble Metal Nanoparticles, *J. Phys. Chem. B* **108**, 109-116 (2004).
10. S. Underwood and P. Mulvancy, Effect of the Solution Refractive Index on the Color of Gold Colloids, *Langmuir* **10**, 3427-3430 (1994).
11. A. J. Haes, S. Zou, J. Zhao, G. C. Schatz, and R. P. Van Duyne, Localized Surface Plasmon Resonance Spectroscopy near Molecular Resonances, *J. Am. Chem. Soc.* **128**, 10905-10914 (2006).
12. S. Eustis and M. A. El-Sayed, Why gold nanoparticles are more precious than pretty gold: Noble metal surface plasmon resonance and its enhancement of the radiative and nonradiative properties of nanocrystals of different shapes, *Chem. Soc. Rev.* **35**, 209-217 (2006).
13. A. J. Haes, S. Zou, G. C. Schatz, and R. P. Van Duyne, Nanoscale Optical Biosensor: Short Range Distance Dependence of the Localized Surface Plasma Resonance of Noble Metal Nanoparticles, *J. Phys. Chem. B* **108**, 6961-6968 (2004).
14. C. J. Murphy, T. K. Sau, A. M. Gole, C. J. Orendorff, J. Gao; L. Gou, S. E. Hunyadi, T. Li, Anisotropic Metal Nanoparticles: Synthesis, Assembly, and Optical Applications, *J. Phys. Chem. B* **109**(29), 13857-13870 (2005).

Chapter 3

A Novel Approach to the Synthesis of Nanochanneled Nickel Films

3. 1 Introduction

Nanoporous metallic membranes have attracted significant interest owing to their wide range of technological applications including catalysis,[1-3] sensing,[1,4] microfluidic flow control[2], and surface enhanced Raman scattering,[1,5-6] among others. The ability to control the pore size and thickness of nanoporous metallic films can optimize the catalytic effects of fuel cells.[1-2] In this case, conversions depend on kinetics or mass transport rather than diffusion.[1] Ultrathin (about 100 nm thick) nanoporous membranes may overcome the limitation of high CO oxidation generation during the catalytic reactions at the surface of a nanoporous metallic film.[1] In addition, large pore size membranes can be used to control microfluidic flow, while small pore size membranes can be employed as sensor materials due to their high specific surface areas.[2] However, these membranes are very fragile and exhibit brittle fracture, which limit their possible applications in flow through type catalysis.[1,3,7]

Nanoporous nickel films have attracted significant attention due to the high electrochemically active surface area to volume ratio, resulting in structures that may have extensive application in fuel cell and battery technologies.[8-11] I report here on a novel method to fabricate relatively thick (0.5 μm and larger) nanochanneled Ni membranes by depositing nickel onto an anodic aluminum oxide (AAO) nanporous substrates with vertically aligned nanochannels. For nickel membrane thickness of about 0.7 μm or smaller, the as-deposited material is nanoporous, with the nanopores in the form of nanochannels aligned with those of the substrate. For thicker membranes, the as-deposited nickel becomes continuous, and a template-guided electrochemical etching technique[12] was used to produce the nanochannels. This physical vapor deposition followed by electrochemical etching approach represents a relatively simple manufacturing method for producing high quality nanoporous metallic membranes for technological applications. It is noted that there have been some reports on the fabrication of nanoporous replicated films using polymethyl methacrylate (PMMA) as the replication medium injected into the nanopores of an anodic aluminum oxide (AAO) membrane under vacuum conditions.[14-17] The disadvantages of this replication method are the incompletion of the replication of the nanoporous features of AAO membranes and the difficulty of injecting the replication medium under vacuum, resulting in the obstacles for applying this method to industrial manufacturing processes. The approach reported here of overlayer deposition onto a nanoporous substrate, followed by electrochemical etching through the substrate to produce a thick metallic nanoporous metallic membrane, represents a simple and robust manufacturing process that can be more easily scaled-up for industrial purposes compared to other fabrication methods.

It is also noted that nanoporous materials usually are fabricated by chemical dealloying using high concentration of acids such as nitric acid or hydrochloric acid and strong bases such as KOH to selective dissolution of less noble elements of an alloy.[2-4,8,19-20] The method presented here is much more environmental friendly than typical methods to produce nanoporous materials because it does not involve these of any corrosive substance in the process.

3.2 Experimental

Anodic aluminum oxide (AAO) nanoporous membranes (Whatman, porosity: ~ 40%) of about 60 μm thickness and pore size of about 100 nm were used as substrates. Physical vapor deposited nickel overlayers were produced by electron beam evaporation or by magnetron sputtering, using a deposition rate of about 0.1 nm/sec in each case. For overalyers of thickness of about 0.7 μm or less, the as-deposited materials was nanoporous, and the membranes were made free-standing by dissolving the AAO substrate in a 4 M aqueous sodium hydroxide (NaOH) solution at room temperature for 2 hours, followed by rinsing in deionized water and ethanol.

For nickel membranes that were sputter deposited at a thickness of greater than about 0.7 μm, the metal overlayers were continuous. In order to produce the nanochannels in the nickel, substrate-guided electrochemical etching was carried out using a constant voltage of 0.1 V vs. a nickel strip as the reference electrode for 1 hour. The electrolyte used in the electrochemical process was a 0.25 M nickel sulfate hexahydrate (Sigma Aldrich, ACS reagent, 99%, 227676-500G), 0.1 M boric acid (Alfa Aesar, 99.99%, metal basis, CAS#10043-35-3), 0.004 M $NiCl_2$ (Sigma Aldrich, 98%,

339350-250G), 0.1 g/L sodium dodecyl sulfate (SDS) (Sigma Aldrich, for molecular biology, L4390-100G), and 0.02 g/L coumarin 6 (Sigma Aldrich, 98%, 442631-5G) aqueous solution. As with the thinner overlayers, the nickel membranes were made free-standing by dissolving the AAO substrate in a 4M aqueous sodium hydroxide solution at room temperature for 2 hours, followed by rinsing in deionized water and ethanol.

3.3 Results and Discussion

The AAO nanoporous membranes used in this work exhibited hexagonally arranged nanoporous arrays with a pore diameter of about 100 nm and a pore spacing of about 150 nm. A plan-view scanning electron micrograph (SEM) image of a nanochanneled nickel of about 0.5 μm thick fabricated by electron beam evaporation deposited onto a nanoporous AAO substrate is shown in Figure 3.1(a). The degree of ordering and planar density of the nanochanneled nickel observed was similar to that of the anodic aluminum oxide templates, strongly suggesting that the AAO substrate nanochannels acted as a template for the formation of the nanochannels in the nickel. The pore diameters ranged from about 50 nm to 250 nm, compared to the substrate diameter of 100 nm. It is also noted that many nanosized features were formed at the inside walls of the nanochannels, resulting in a very large effective surface area.

Figure 3.1(b) shows a plan-view SEM image of nickel membrane of about 0.5 μm thickness produced by sputtering. Compared to the membrane of approximately the same thickness produced by evaporation, the sputtered membrane resulted in significantly smaller diameter nanochannels coupled with an increase in the planar density of the

nanochannels. This microstructure can be explained by an incomplete filling, followed by an incomplete agglomeration, within the initially growing nanochannels.

A plan view SEM micrograph of a sputtered Ni overlayer of about 1.5 μm thickness onto an AAO membrane is shown in Figure 3.2. It is seen that the nickel deposit at the end of deposition was continuous. Figures 3.3(a) and 3.3(b) show, respectively, plan-view and cross-sectional SEM micrographs of the nanochanneled Ni membrane formed after the sample shown in Figure 3.3 was electrochemically etched. During the etching, the nanoporous AAO substrate acted as a mask so that only the nickel over the pores of the AAO was exposed and only the nickel in the vicinity of these pores was etched. The nanochanneled patterning of the AAO template was completely transferred to the Ni membrane, and the resulting in approximately the same pore diameter (about 100 nm).

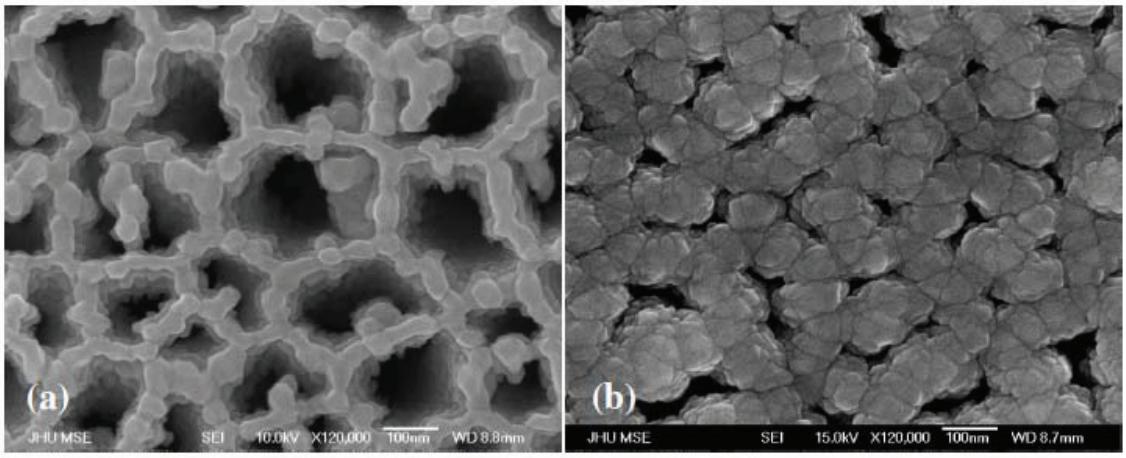

Figure 3.1 SEM micrograph of nickel nanochanneled membranes deposited onto nanoporous AAO substrates by (a) electron beam evaporation; (b) sputtering. Both membranes have a thickness of about 0.5 μm and were deposited at a rate of ~ 0.1 nm/sec.

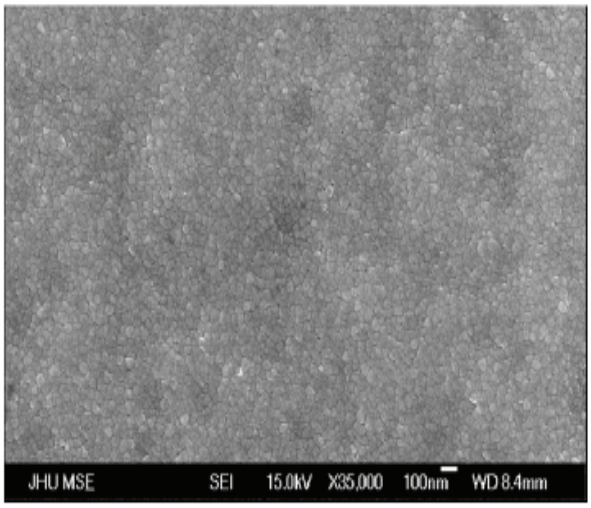

Figure 3.2 SEM micrograph of sputtered Nickel surface. The thickness of film is 1.5 μm.

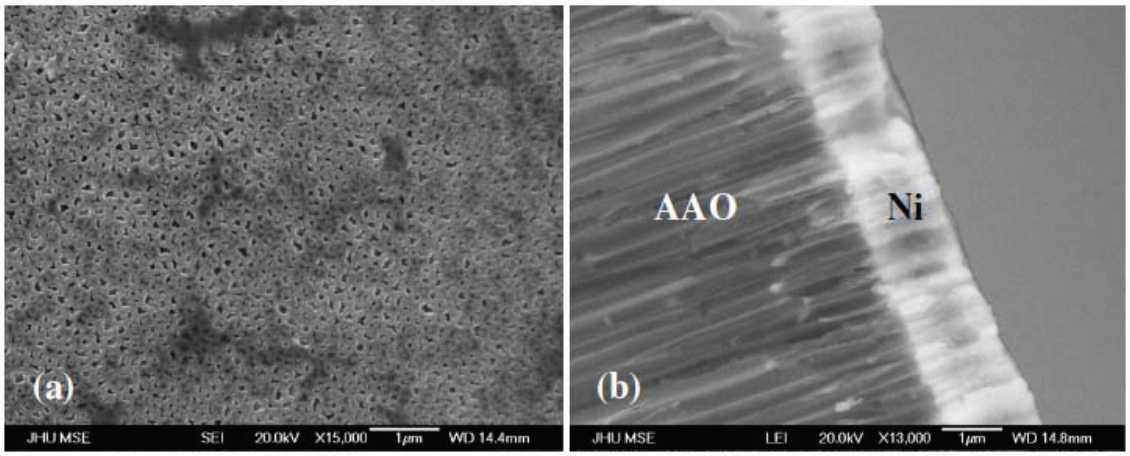

Figure 3.3 (a) Plan-view and (b) cross-sectional SEM micrographs of a nickel nanochanneled membrane produced after electrochemical etching through the AAO substrate of the sample in Figure 2. The pore size is about 100 nm, same as the AAO substrate.

3.4 Conclusions

A novel and relatively simple approach for the synthesis of nanochanneled metal membranes with different pore sizes and inter-pore distance has been presented. Nickel nanoporous membranes of thickness less than about 0.7 μm were produced by physical vapor deposition of nickel overlayers by either electron beam evaporation or sputtering onto anodic aluminum oxide nanoporous substrates with vertically aligned nanochannels. The resulting overlayers were nanoporous, with the nanopores in the form of nanochannels aligned with the nanochannels of the substrate. In the case of the evaporated membranes, the pores had diameters within a factor of 2.5 of that of the substrate (100 nm) and a similar planar density, suggesting that the substrate acted as a template for the nanoporous nickel. The sputtered nickel also was deposited as a nanoporous material, but with a greater density of pores and smaller pore diameters, suggesting partial filling and incomplete agglomeration within the initially formed pores. For sputtered overlayers of thickness 0.7 μm or greater, the deposited metal became

continuous, and electrochemical etching through the AAO substrate was used to on these samples to produce the nanochannels. For all of the samples, the substrate could be completely dissolved, resulting in free-standing metallic membranes.

3.5 Future Work

The nanosized features from the cross-sectional view of nanochanneled nickel membrane can be investigated by SEM. The nanochanneled membranes with different pore sizes can be fabricate and the morphology of the various pore size membranes will also be examined by SEM. Large pore size membranes could be used to control microfluidic flow, whereas small pore size memebranes could be employed as sensor materials due to their high specific surface areas. If the pore size can be made to less than 20 nm, it is worthwhile to also test possible catalytic effects.

Bibliography

1. L. Liu, W. Lee, Z. Huang, R. Scholz, and U. Gosele: Fabrication and characterization of a flow through nanoporous gold nanowire/AAO composite membrane. *Nanotechnology* **19**, 335604 (2008).
2. Y. Ding and J. Erlebacher: Nanoporous metals with controlled multimodal pore size distribution. *J. Am. Chem. Soc.* **125**, 7772 (2003).
3. Y. Ding, Y. J. Kim, and J. Erlebacher: Nanoporous gold leaf: "ancient technology"/ advanced material. *Adv. Mater.* **16**, 1897 (2004).
4. Z. Liu and P. C. Searson, Single nanoporous gold nanowire sensors. *J. Phys. Chem. B* **110**, 4318 (2006).
5. S. O. Kucheyev, J. R. Hayes, J. Biener, and T. Huser: Surface-enhanced Raman scattering on nanoporous gold. *Appl. Phys. Lett.* **89**, 053102 (2006).
6. L. H. Qian, X. Q. Yan, T. Fujita, A. Inoue, and M. W. Chen: Surface enhanced Raman scattering of nanoporous gold: smaller pore sizes stronger enhancements. *Appl. Phys. Lett.* **90**, 153120 (2007).
7. C. X. Xu, J. X. Su, X. H. Xu, P. P. Liu, H. J. Zhao, F. Tian, and Y. Ding: Low temperature CO oxidation over unsupported nanoporous Gold. *J. Am. Chem. Soc.* **129**, 42 (2007).
8. J. Cai, J. Xu, J. Wang, L, Zhang, H. Zhou, Y. Zhong, D. Chen, H. Fan, H. Shao, J. Zhang, and C.-N. Cao, Fabrication of three-dimensional nanoporous nickel films with tunable nanoporosity and their excellent electrocatalytic activities for hydrogen evolution reaction, *International Journal of Hydrogen Energy* **38**, 934-941 (2013).

9. J. Cabana, Z. Stoeva, J. J. Titman, D. H. Gregory, M. Rosa Palacin, Towards new negative electrode materials for Li-ion batteries: electrochemical properties of LiNiN. *Chem. Mater.* **20**, 1676-1678 (2008).
10. O. A. Marina, L. R. Pederson, C. A. Coyle, E. C. Thomsen, P. Nachimuthu, and D. J. Edwards, Electrochemical, structural and surface characterization of nickel/zirconia solid oxide fuel cell anodes in coal gas containing antimony, *J. Power Sources* **196**, 4911-4922 (2011).
11. C. A. Marozzi and A. C. Chialvo, Development of electrode morphologies of interest in electrocatalysis. Part 1: electrodeposited porous nickel electrodes, *Electrochem. Acta.* **45**, 2111-2120 (2000).
12. Yan-Yan Gao, Ai-Juan Han, Fang Miao, Guang-Lan Li, Hui Li, Zuo-Shan Zhang, and Shu-Yong Zhang: Preparation of metallic nanopore arrays using template-guided electrochemical etching, *Mater. Lett.* **64**, 1028-1030 (2010).
13. K. Nice and J. Strickland, How Fuel Cells Work, September 18, 2000. HowStuffWorks.com. URL:http://auto.howstuffworks.com/fuel-efficiency/alternative-fuels/fuel-cell.htm
14. H. Masuda, K. Nishio, and N. Baba, Fabrication of Porous TiO2 Films Using Two-Step Replication of Microstructure of Anodic Alumina, *Jpn. J. Appl. Phyc*. **31**, L1775-L1777 (1992).

15. H. Masuda and K. Fukuda, Ordered Metal Nanohole Arrays Made by a Two-Step Replication of Honeycomb Structures of Anodic Alumina, *Science* **268** (5216), 1466-1468 (1995).
16. P. Hoyer, N. Baba, and H. Masuda, Small quantum-sized CdS particles assembled to form a regularly nanostructured porous film, *Appl. Phys. Lett.* **66**, 2700 (1995).
17. Y. Lei, W.K. Chim, Z. Zhang, T. Zhou, L. Zhang, G. Meng, and F. Phillipp, Ordered nanoporous nickel films and their magnetic properties, *Chem. Phys. Lett*. **380**, 313-318 (2003).
18. D. Mukherji, G. Pigozzi, F. Schmitz, O. Näth, J. Rösler, and G. Kostorz, Nano-structured materials produced from simple metallic alloys by phase separation, *Nanotechnology* **16**, 2176 (2005).
19. C. Ji and P. C. Searson, Synthesis and Characterization of Nanoporous Gold Nanowires, *J. Phys. Chem. B* **107** (19), pp 4494–4499 (2003).
20. F. Jia, C. Yu, K. Deng, and L. Zhang, Nanoporous Metal (Cu, Ag, Au) Films with High Surface Area: General Fabrication and Preliminary Electrochemical Performance, *J. Phys. Chem. C* **111**, 8424-8431 (2007).

Chapter 4

Purification and Refinement of Single-Walled Carbon Nanotubes (SWCNTs) by AC Dielectrophoresis

4.1 Introduction

Since the success of integrated silicon technology of metal oxide semiconductor field-effect transistor (MOSFET), the ability to scale down the dimensions of the device has been the key to improving speed and energy efficiency.[1-2] However, industry generally expects that fundamental material barriers will limit the size reduction of current nanoscale MOSFET devices and that this road block to continuing advancement will arrive within a decade as predicted by Moore's law.[2] In order to overcome these barriers, new materials are needed to solve the scalability problems of future silicon devices. Among these new silicon substitute materials, single-walled carbon nanotubes (SWCNTs) have become excellent candidates as building blocks for future nanoscale electronics due to their small size and unique electrical properties. In 2012, the New York Times reported on the future of single-walled carbon nanotubes (SWCNTs) as a successor of silicon. IBM's director of physical sciences, Dr. Supratik Guha, at the

company's Yorktown Heights, NY research center was quoted as saying that "these carbon nanotube based devices outperformed any other switches made from any other material, including silicon."[3]

SWCNTs have been actively pursued as electronic materials and silicon device substitutes since Ijima and Bethune independently discovered them in 1993.[1-2,4-5] However, current SWCNT production techniques generate a mixture of two types of nanotubes with divergent electrical behaviors. Some of the nanotubes act as metallic materials, while others display semiconducting properties. This as-synthesized random mixture has complicated the realization of functional carbon nanotube-based nanoelectronics.[4,6-7] Here we report a method of separating metallic SWCNTs from semiconducting ones from an initially random mixture of SWCNTs in suspension using AC dielectrophoresis (DEP). The goal of this project is to fabricate a microfluidic lab-on-a-chip device that can continuously purify, sort and collect industrially relevant quantity of metallic and semiconducting SWCNTs.

This technique separates metallic SWCNTs from semiconducting ones due to the difference in the magnitude and direction of dielectrophoretic forces experienced by the two types of nanotubes. The large difference in force is related to the fact that metallic SWCNTs display a large absolute dielectric constant and semiconducting SWCNTs display a corresponding low value, as reported by Krupke and co-workers.[4] It is noted that sorted SWCNTs have great commercial value. Currently, sorted 98% pure semiconducting nanotubes cost $520 per mg and sorted 98% pure metallic tubes cost $788 per mg.[8]

4.1.1 Single-Walled Carbon Nanotubes (SWCNTs)

A single-walled carbon nanotube (SWCNT) can be considered to be a single rolled-up graphene sheet with its ends folded to form a seamless hollow cylinder.[9] SWCNTs are nanostructures with dimensions of about 1 nm in diameter and lengths are about a few microns to centimeter range.[10] A SWCNT can be mathematically represented as the chiral vector, C. The definition of the chiral vector comes from treating the circumference of a nanotube as two crystallographically equivalent sites of a two-dimensional (2-D) grapheme sheet.[11] The chiral vector, *C*, is written as

$$C = na_1 + ma_2, \tag{4.1}$$

where (*n*, *m*) are integers called chiral vector and a_1 and a_2 are unit vectors of the hexagonal honeycomb lattice. For example, a (4, 4) chiral vector nanotube is described in Figure 4.1.[11] Chiral vectors can also be related to the electronic types of SWCNTs as shown in Figure 4.2. SWCNTs exhibit either metallic or semiconducting behaviors depending on diameter and orientation of carbon hexagons with respect to the tube axis (degree of chirality).[9,13] Dresselhaus *et al.* reported that when $n - m = 3q$, SWCNTs can be classified as metallic tubes due to the change of singularities in the 1D density of states as determined from a quasi-continuum and theoretical calculation.[14-15] On the other hand, SWCNTs is semiconducting when $n - m \neq 3q$, where q is an integer in both cases.[9,13-15] In general, the diameter of a SWCNT can be mathematically represented in terms of integers (n, m) as

$$d_t = \frac{C_h}{\pi} = \frac{\sqrt{3}a_{C-C}\sqrt{m^2+mn+n^2}}{\pi}, \tag{4.2}$$

where $a_{C\text{-}C}$ is the nearest neighboring center to the center distance of C-C bonds (~ 1.42Å for graphite) and C_h is the length of a chiral vector.[16]

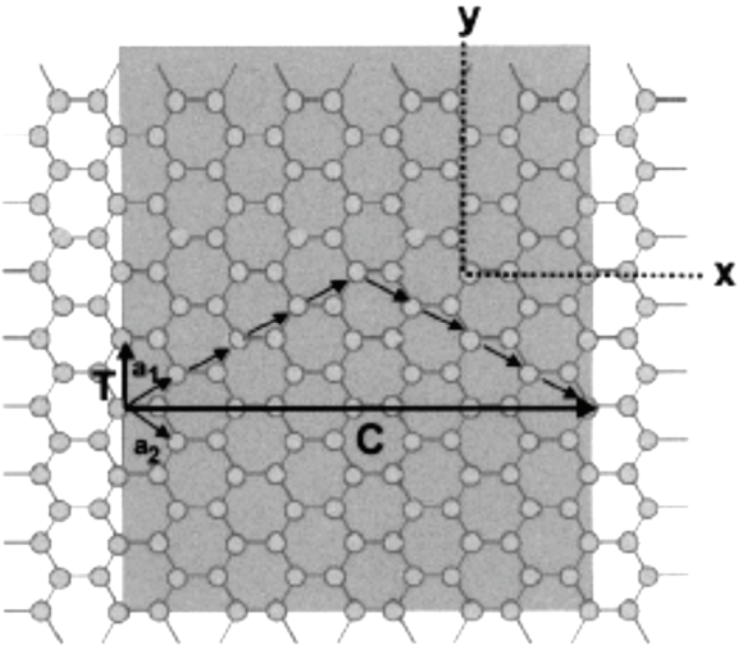

Figure 4.1 the structure a SWCNT in terms of its chiral vector. Figure reprinted from *Proceedings of the IEEE***.** Vol. 91, No. 11 (2003). Copyright 2003, IEEE.

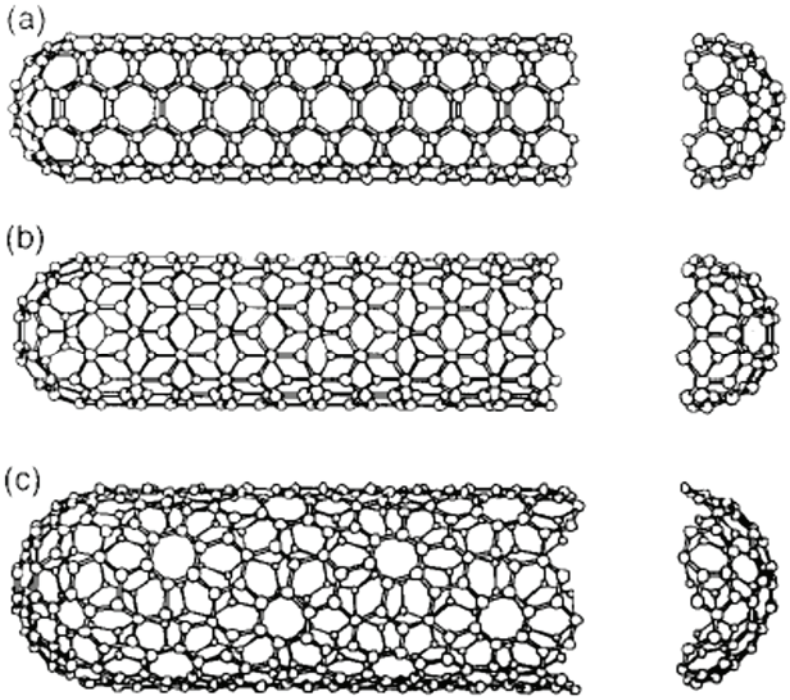

Figure 4.2 Schematic of SWCNTs exhibited both metallic and semiconducting behaviors depending on diameter and orientation of carbon hexagons with respect to tube axis (degree of chirality). (a) an "armchair" metallic nanotube (5,5), (b) a "zigzag" metallic nanotube (9,0), and (c) a "chiral" semiconducting nanotube (10,5).[13] Figure reprinted from *Carbon* **33** (7), 883-891 (1995). Copyright 1995, Elsevier Science Ltd.

SWCNTs are a very good thermal conductive material along the tube axis. They exhibit a property known as "ballistic (scattering free) conduction." Measurements show that a SWNT has a room temperature thermal conductivity along its axis of about 3500 $W \cdot m^{-1} \cdot K^{-1}$.[17] Copper, a metal well known for its superior thermal conductivity, has a room temperature thermal conductivity of 385 $W \cdot m^{-1} \cdot K^{-1}$. Therefore, a SWCNT can conduct 10 times more heat than a copper along its tube axis at a room temperature. SWCNTs are also good insulators laterally to the tube axis. A SWNT has a room-temperature thermal conductivity across its axis (in the radial direction) of about 1.52 $W \cdot m^{-1} \cdot K^{-1}$, which is about as thermally conductive as soil.[18] Furthermore, due to the strong Carbon-Carbon covalent bond in SWCNTs lead to enhanced mechanical

properties. SWCNTs have Young's modulus about ten times higher than that of steel. This strong covalent bonding also leads to the near defect free structure of SWCNTs.[11] SWCNTs are also chemical inert to most of solvent and carbon is a very light weight material.

In addition, variability during production of SWCNTs leads to tubes of different diameter and atomic configuration relative to the tube axis (degree of chirality).[2,9] These structural variations dictate the electronic properties of SWCNTs and can result in metallic or semiconducting nanotubes as shown in Figure 4.2. It is known that approximately $\frac{2}{3}$ of the SWCNTs are semiconducting and about $\frac{1}{3}$ of the SWCNTs are metallic from a single production.[9,12] The metallic behavior of SWCNTs comes from the small opening energy gap at the Fermi level due to the curvature of the graphene sheet.[14] Since SWCNTs are 1-D systems resulting reduced phase space for electron carrier scattering, the tubes have much lower resistivity than 3-D structures. Therefore, energy dissipation of a semiconducting SWCNT is minimal. As a result, semiconducting SWCNTs have the advantage to use carbon nanotubes in field-effect transistor (FET) technologies. Meanwhile, metallic SWCNTs can carry current densities 2 to 3 orders of magnitude higher than Cu or Al, such as 10^9 A/cm^2.[19] The unique properties can allow metallic SWCNTs to be a good candidate of interconnect of nanoelectronics.[20-21]

However, with so many excellent and unique, mechanical, chemical, thermal, and electronic properties, there are challenges in producing SWCNT-based devices. The main reason is that there is no known synthesis method that can control SWCNTs with similar diameters and electronic properties as determined by chirality. The current technology can only produce polydisperse SWCNTs with different chirality. Therefore, it is

important and more efficient to develop effective purification and separation methods until the controllable synthesis method is achieved, whether separating by metallic from semiconducting, sorting by diameter, or in terms of chirality. In this chapter, the focus will be to address on the fabrication a microfluidic device that can continuously collect and sort the initial mixed electronic types of SWCNTs into individual groups of refined metallic or semiconducting SWCNTs. By doing so, this separating device can be used as a very effective tool to scale up the supply of refined and purified metallic or semiconducting SWCNTs to an industrial relevant quantity in order to make CNT-based electronics to reach commercial reality.

4.1.2 AC Dielectrophoresis on Single-Walled Carbon Nanotubes

Dielectrophoresis (DEP) is an electro-kinetic phenomenon where a non-uniform electric field induces polarization in a neutrally charged particle and causes motion of the induced dipole.[8] That is, in an AC and nonuniform electric field, depending on the polarizability of the particle compared to that of the medium, the dielectrophoretic (DEP) force could push the material toward the direction of the electric field gradient (positive DEP force) or against field gradient (negative DEP force).[22-24] The dielectrophoretic force exerted on a polarized particle in a nonuniform electric field in suspension can be written as:

$$F_{DEP} = (\boldsymbol{p} \cdot \nabla)\boldsymbol{E}, \tag{4.3}$$

where $\boldsymbol{p}$ is the induced dipole moment and $\boldsymbol{E}$ is the electric field. In an AC field, the polarized particle exhibits frequency dependent behavior.[25-26] Here a long and thin carbon nanotube is approximated as a prolate ellipsoid. The DEP force can be represented by:

$$F_{DEP} = \frac{\pi r^2 l}{2} \boldsymbol{\varepsilon_m} Re(K) \nabla |\boldsymbol{E}|^2 \tag{4.4}$$

$$K = \frac{\boldsymbol{\varepsilon_p^* - \varepsilon_m^*}}{\boldsymbol{\varepsilon_m^* + L(\varepsilon_p^* - \varepsilon_m^*)}} \tag{4.4}$$

$$\boldsymbol{\varepsilon^* = \varepsilon - j\frac{\sigma}{\omega}} \; and \; L = \frac{ln\left(\frac{l}{r}\right) - 1}{\left(\frac{l}{2r}\right)^2}, \tag{4.5}$$

where K is the Claussius-Mossotti factor, $\boldsymbol{\varepsilon^*}$ is the complex dielectric constant, $\boldsymbol{\varepsilon}$ is the relative permittivity (dielectric constant), $\boldsymbol{\sigma}$ is the conductivity, $\boldsymbol{j} = \sqrt{-1}$, and $\boldsymbol{\omega}$ is the frequency of the AC electric field; the subscripts $\boldsymbol{p}$ and $\boldsymbol{m}$ refer to the particle and the medium in which it is suspended.[25-28] l is the length of the particle, r is the radius of the particle and L is a shape factor.

The equation of a translational motion of a SWCNT (modeled as a prolate ellipsoid) in a viscous medium is governed by Newton's second law:

$$m_{CNT} \frac{dV_{CNT}}{dt} = F_{DEP} + f(v_{CNT} - v_m), \tag{4.6}$$

where m_{CNT} is the mass of a SWCNT, v_{CNT} is the translational velocity of a SWCNT, f is the fraction factor which depends on the particle geometry and the fluid viscosity, and v_m is the velocity of the viscous medium. The solution of equation (4.5) was developed by Morgan and Green.[24] When the initial SWCNT velocity is zero, the velocity of a SWCNT can be taken as:

$$v_{CNT} = \left(\frac{F_{DEP}}{f} + v_m\right)\left(1 - e^{-\frac{f}{m_{CNT}}t}\right). \tag{4.7}$$

Since for a nanosized particle, the characteristic time, τ $(= \frac{m_{CNT}}{f})$, is a very small number. The velocity of a SWCNT in a viscous medium is given by

$$v_{CNT} \approx \left(\frac{F_{DEP}}{f} + v_m\right). \tag{4.8}$$

For two particles with the same geometry, in the same medium, and under the same electric field conditions, any difference in direction and magnitude of the DEP force is determined by the real part of the Claussius-Mossotti factor, *Re(K)*:

$$Re(K) = \frac{\epsilon_p\epsilon_m + L\epsilon_p^2 - \epsilon_m^2 + \frac{\sigma_p\sigma_m - \sigma_m^2 + L\sigma_p^2}{\omega^2}}{\left(\epsilon_m + L\epsilon_p\right)^2 + \left(\frac{L\sigma_p + \sigma_m}{\omega}\right)^2}. \tag{4.9}$$

At high frequencies (ω), the Claussius-Mossotti factor is determined by the permittivity of different types of SWCNTs and the medium.[22,25-28] From Equation (4.10) and (4.11), one can identify *Re(K)* and the DEP force in the high frequency limit,

$$\lim_{\omega\to\infty} Re(K) = \frac{\epsilon_p\epsilon_m + L\epsilon_p^2 - \epsilon_m^2}{(\epsilon_m + L\epsilon_p)^2}$$

$$\lim_{\omega\to\infty} F_{DEP} = \frac{\pi r^2 l}{2}\epsilon_m \frac{\epsilon_p\epsilon_m + L\epsilon_p^2 - \epsilon_m^2}{(\epsilon_m + L\epsilon_p)^2}\nabla|E|^2 \quad . \qquad (4.10, 4.11)$$

Therefore, depending on the polarizability of a nanostructure compared to that of the medium, the electrophoretic force could push the nanotubes toward the high electric field density region (positive dielectrophoresis) or the low electric field density region (negative dielectrophoresis).[22-24,29] By tuning the AC field to a particular frequency, it is possible to drive the metallic tubes in the direction of the electric field gradient while simultaneously driving the semiconducting tubes against the field gradient resulting in segregation of the mixture. The gradient of the electric field in this experiment is generated by the non-uniform shape of the electrodes.

One can see that based on Equation (4.10) as the AC field frequency driven to a high limit, the value of *Re(K)* will be positive when $\varepsilon_p\varepsilon_m + L\varepsilon_p^2 > \varepsilon_m^2$ and the value of *Re(K)* will be negative when $\varepsilon_p\varepsilon_m + L\varepsilon_p^2 < \varepsilon_m^2$. The reported relative permittivity and conductivity of a metallic SWCNT are $10^4\varepsilon_0$ (where ε_0 is the permittivity of free space, 8.85 x 10^{-12} F/m) and 10^8 S/m, respectively.[25] For a semiconducting SWCNT, relative permittivity and conductivity are $2.5\varepsilon_0$ and 10^5 S/m.[25] The reported relative permittivity

and conductivity of the medium (deionized water with SDS surfactant) used in the experiment are $80\varepsilon_0$ and 10^{-3} S/m.[30] From these reported relative permittivity and conductivity, one can estimate that the metallic SWCNTs will experience a positive DEP force because of the positive *Re(K)* value and the semiconducting SWCNTs will experience a negative DEP force due to the negative *Re(K)* value. One important note is that the medium can be changed to adjust the permittivity and conductivity to tailor the DEP effect acting on carbon nanotubes. In addition, if *Re(K)* crosses 0, the crossover frequency can be defined as:

$$\omega_{cross} = \sqrt{\frac{\sigma_p \sigma_m + L\sigma_p^2 - \sigma_m^2}{\epsilon_m^2 - \epsilon_p \epsilon_m - L\epsilon_p^2}} \quad . \tag{4.12}$$

4.1.3 Understanding Electronic Types of SWCNTs from their Resonant Raman Features

Resonant confocal micro Raman spectroscopy (RCMRS) has become a powerful technique to study the electronic properties and vibrational behaviors of SWCNTs.[31-32] For both metallic and semiconducting SWCNTs, when a laser excitation energy caused Raman scattering by phonons is in resonance with an electronic transition with an energy E_{ij} for which there is a strong optical absorption due to the energy jump between the valence and conduction bands,[10,12] where the subscript *i* is denoted as the valence subband edge and *j* is denoted as the conduction subband edge. The strong resonance

condition allows scientists and engineers to obtain large Raman signaling enhancements due to this enhanced coupling between electrons and phonons of SWCNTs.

Two features of signature wavenumbers of Raman spectra are used to identify the electronic properties of SWCNTs. The radial breathing mode (RBM) represents the laser excited vibration of carbon atoms in phase in the radial direction relative to the nanotube axis.[9] The radial breathing mode (RBM) region usually occurs at the frequencies of 100 to 350 cm^{-1} for SWCNTs[31] and according to Araujo *et al.* and Dresselhaus *et al.*, the RBM frequency, ω_{RBM}, is depended on the reciprocal of the carbon nanotube diameter, d_t.[10,32-35]

$$\omega_{RBM} = \frac{A}{d_t} + B, \tag{4.13}$$

where A and B are constants and vary between individual tubes and bundle tubes from experimental observations.[16,33-34,36] The constant A is also in the diameter determination.[20,47] The RBM frequency is independent of the chiral angle.[9]

Metallic SWCNTs have RBM wavenumbers in the range of 220 - 300 cm^{-1} with a laser excitation wavelength of 514.5 nm (2.41 eV). Semiconducting SWCNTs have RBM wavenumbers in the range of 170 - 220 cm^{-1} with a laser excitation wavelength of 514.5 nm.[10,29,37] The wavenumbers of RBM peaks also provide information on chirality, which is related to the electronic properties of SWCNTs. Li *et al.* summarized this reciprocal dependence between RBM frequency and carbon nanotube diameter is valid when the tube diameter is larger than 0.7 nm.[38] However, when the diameter of a SWCNT is

getting smaller, the reciprocal dependence will become invalid due to the induced curvature effect.[38-39]

The G-band mode (tangential mode) is related to vibrations in all sp^2 carbon materials.[36] The characteristic Raman features and lineshape of the G-band mode corresponds to the electronic properties (semiconducting or metallic) of SWCNTs.[16] In general, as shown in the reference Raman spectra in Figure 4.11, the Raman spectra of semiconducting SWCNTs show a sharp peak at 1592 cm^{-1} for the G-band mode, while metallic SWCNTs generate a broad peak at 1582 cm^{-1} for the G-band mode.[9,16,29,31,37,40-41] The G band is also reported to be constructed by two components, the lower frequency component associated with vibrations along the circumferential direction (G^-) and the higher frequency component attributed to vibrations along the direction of the tube axis (G^+).[36]

Since the response for laser excitation with varied wavelength reveal very different Raman spectra for each sample,[41-43] the Kataura plot is used to relate different laser excitation levels to the diameter of SWCNTs and the Raman shift wavenumber of corresponding resonance scattering nanotubes.[44] One important note is that according to the Kataura plot, there is a possibility that a single SWCNT can be evaluated as a metallic or semiconducting nanotubes by using different energy lasers. Therefore, significant errors may occur if one does not carefully use the same wavelength laser in the experiment because each analysis can give different optical properties.

4.2 Experimental

4.2.1 Static System

This section is an adapted reproduction from Su Chih Chi, Robert C. Cammarata, Chia-Ling Chien, Donglei Fan, Stephen Farias, and Danru Qu, inventors, Johns Hopkins University, assignee, "Systems and Methods for Separating Metallic and Nonmetallic Particles in a Mixed-Particle Suspension," U. S. Patent Provisional Application No. 13/902,191, Filling date: May 24, 2013.

Single-walled carbon nanotubes (SWCNTs) purchased from Sigma-Aldrich (carbon > 90%, ≥ 70% carbon as SWCNT) were used in this study. Suspensions were prepared by mixing 2 mg of raw SWCNTs roots in 20 ml deionized water with 1 wt.% of the surfactant sodium dodecyl sulfate (SDS) (99.0%, Sigma-Aldrich). The suspension was ultra-sonicated for 30 minutes and then centrifuged at 3000 rpm for 2 hours. The upper 80% of the suspension was taken to use in the experiment. To obtain the non-uniform electric field required for dielectrophoresis, a gold microelectrode (MaxTek, Inc. P/N 149272-1) composed of a circular inner electrode of radius of about 3.3 mm and a semicircular outer electrode of radius of about 9 mm as shown in Figure 1 was used in the experiments. The electrodes provided a radial electric field gradient to establish a radially directed dielectrophoretic force. The SWCNTs separation device is connected to a HP E3617A DC power supply and an Agilent Technologies 33120A 15 MHz function waveform generator. After the function generator was switched on, a drop of suspension (~ 100 μL) was released into the gap between the circular inner and semicircular outer electrodes.

The separation was operated at a frequency of 10 MHz and a peak-to-peak voltage of 10 V_{p-p} between the two electrodes. After the voltage was applied, the suspension was allowed to rest and air dry for ~ 4 hours and samples were collected from each electrode. To confirm the segregation of metallic and semiconducting SWCNTs, resonant Raman spectroscopy was performed since the difference in optical properties between metallic and semiconducting SWCNTs allows the spectral peaks of each species in the Raman data to be resolved distinguishably[16]. The G-band and radial breathing mode (RBM) frequencies of metallic and semiconducting SWCNTs were identified using the Ar^+ ion laser excitation energy of 2.41 eV (514 nm). The Raman spectra at position 1 (SWCNTs are near the circular inner electrode) and position 4 (SWCNTs are near the semicircular outer electrode) were generated by an Ocean Optics QE65000 Raman scientific-grade spectrometer equipped with a Mitutoyo microscope and a thermoelectrically cooled charge-coupled device (CCD). The Raman spectra at position 2 (SWCNTs are about 5 μm away from the circular inner electrode) and position 3 (SWCNTs are about 300 μm away from the circular inner electrode) were generated by a HORIBA Scientific Raman system.

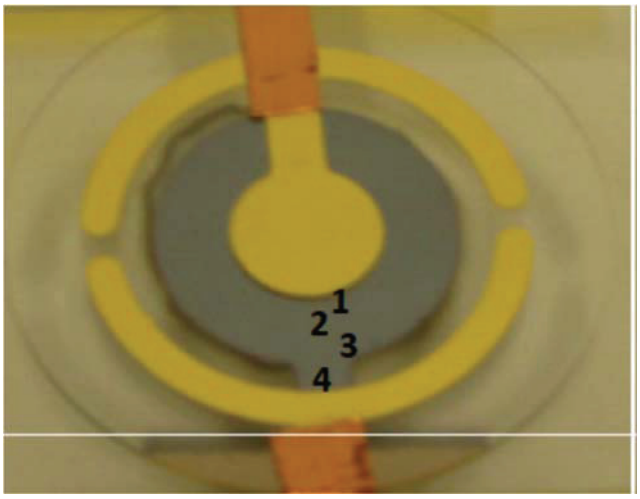

Figure 4.3 Image of electrode setup for separating metallic and semiconducting single-walled carbon nanotubes from a static fluid suspension. The Raman spectra were taken using focused laser spots at positions 1-4 respectively.

4.2.2 Continuous Flow System

The fabrication of the continuous flow device involved two parts: the Au electrodes and microfluidic channels. A standard photolithography process on a Corning glass substrate patterns Au electrodes. The chamber and microfluidic channels are made of an insulating material, polydimethylsiloxane (PDMS), by standard microfabrication techniques. The first component is the Au electrode and the other one is the flow channels made from polydimethylsiloxane (PDMS) polymer. The patterns of both Au electrodes and flow channels used in the experiment were designed by Adobe Illustrator vector-based drawing software. The designed photomasks were then fabricated on transparency films at In Tandem Design, Inc. in Towson, Maryland. Figure 4.4 shows a typical photomask for the Au electrode used in the experiment.

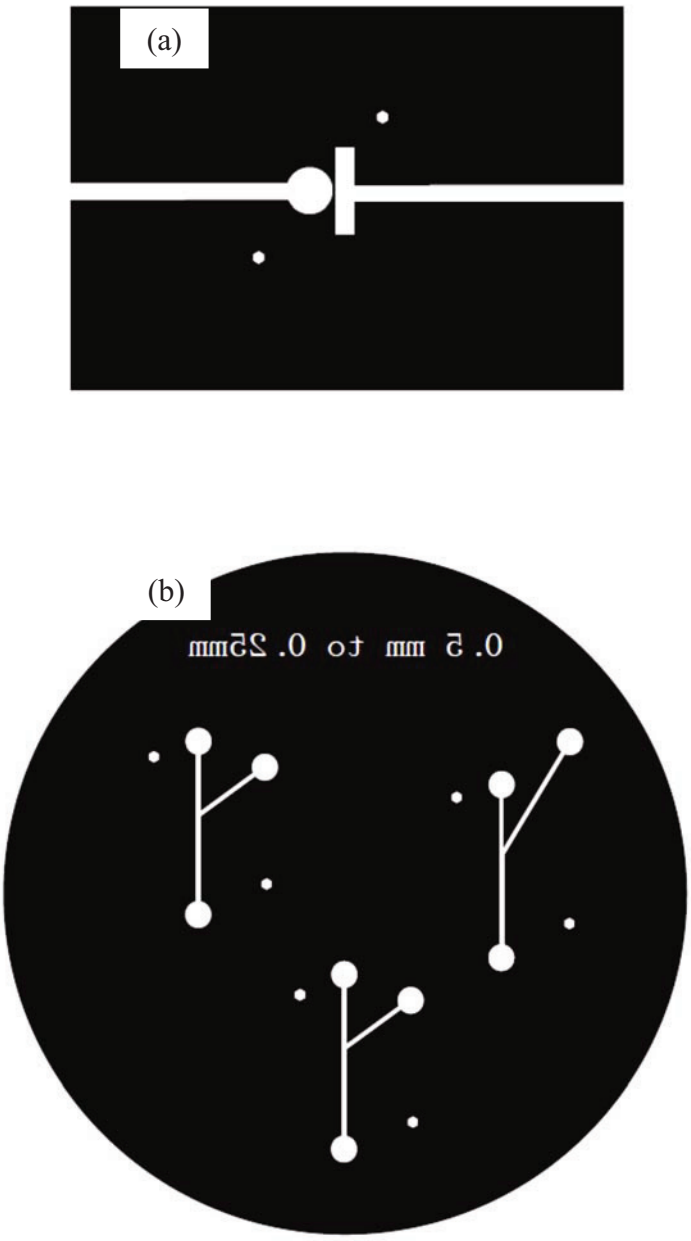

Figure 4.4 Typical photomask for (a) the Au electrode and (b) the flow channels fabricated on a transparency film.

A schematic illustration of the Au electrode fabrication involved in photolithography is shown in Figure 4.5. A 3" x 2" x ½ mm glass slide (Fisher Scientific) was used as the substrate for the Au electrode. The glass slide was first washed and rinsed with acetone and isopropyl alcohol and then blew dry with N_2 gas. The slide was then oxygen plasma cleaned in vacuum for 2 minutes in an oxygen plasma cleaner (Plasma Etch, Inc., Carson, NV USA). Oxygen plasma cleaning was used to remove any extra impurities and contaminants from the surface of the glass slide through the use of energetic oxygen plasma. The surface cleaned glass slide was then spin-coated with AZ5214E image reversal photoresist (Clarient Corporation, Somerville, NJ USA) at 4,000 rpm for 45 seconds. The spin coater (Model PWM32, Headway Research, Inc., Garland, TX USA) was connected to a vacuum pump. The photoresist-coated glass slide was then baked on a hotplate (Thermo Scientific, Waltham, MA USA) for 60 seconds at 115°C. After the glass slide reached to the room temperature, the photoresist was exposed UV light with the photomask with a dosage of 24 mJ/cm^2 for 5 seconds to fabricate the patterns of the relief structures for the gold electrode. An UV mask aligner (OAI Hydralign Series 200, San Jose, CA USA) was used in the photolithography process. The post UV light exposed photoresist was then developed in AZ400K developer (Clarient Corporation, Somerville, NJ USA; AZ400K : deionized water = 1 : 4) for 35 seconds. After the development of the photoresist, the glass slide was rinsed with deionized water for 10 seconds and then blew dry with N_2 gas. Gold (200 nm thick) and Chromium adhesive layer (5 nm thick) was then electron beam evaporated onto the glass slide with the patterned complementary structures using a Kurt J. Lesker PVD75 electron beam

evaporator. The gold electrode pattern was revealed by washing off the photoresist by acetone.

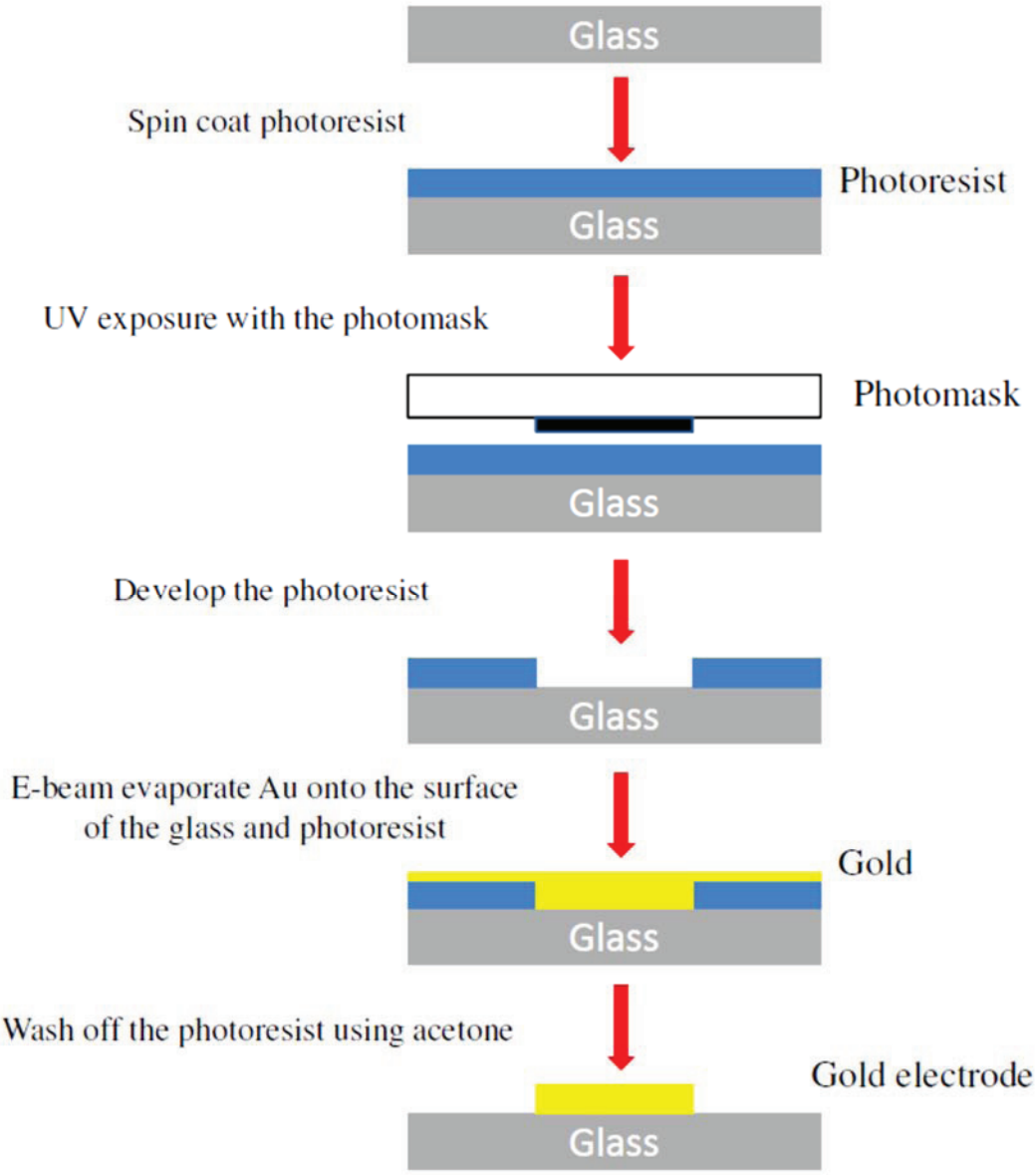

Figure 4.5 Schematic illustration of the Au electrode fabrication involved in photolithography.

The schematic of fabricating the PDMS flow channels are described in the Figure 4.6. A 4 inch silicon wafer (University Wafer, Part# S4P01SP) was used as the substrate for the PDMS flow channels. The silicon wafer was first washed and rinsed with acetone and isopropyl alcohol and then blown dry with N_2 gas. The wafer was then oxygen plasma cleaned in vacuum for 2 minutes in a oxygen plasma cleaner (Plasma Etch, Inc., Carson, NV USA). Oxygen plasma cleaning was used to remove any extra impurities and contaminants from the surface of the wafer through the use of energetic oxygen plasma. The surface cleaned wafer was then spin-coated with SU-8 3025 negative-tone photoresist (Microchem Corp., Newton, MA USA) at 2,000 rpm for 45 seconds, resulting a channel height of ~ 15 μm. The photoresist-coated wafer was then baked on the hotplate for 13 minutes at 95°C. After the wafer reached to the room temperature, the photoresist was exposed UV light with the photomask with a dosage of 24 mJ/cm^2 for 10 seconds to fabricate the patterns of the relief structures for the flow chaneels. The OAI UV mask aligner was used in the photolithography process. After the exposure, the wafer was baked on a hotplate for 1 minute at 65°C and then baked for 4 minutes at 95°C. The post-baked wafer was then developed in SU-8 developer (Microchem Corp. Newton, MA USA) for 7 minutes. After the development, the wafer was rinsed with SU-8 developer for 10 seconds and then rinsed with isopropyl alcohol for 10 seconds. The wafer with was then blown dry with N_2 gas.

PDMS liquid precursor was mixed with 10 parts of Sylgard 184 silicone elastomer base and 1 part of Sylgard 184 silicone elastomer curing agent by weight from Dow Corning. A plastic spoon was used to thoroughly mix the base and the curing agent. Air bubbles were generated in the mixing process. The wafer with the patterned

complementary structures was firstly placed in a Petri dish. Then the liquid PDMS mixture was poured onto the surface of the wafer until the whole surface was covered by the mixture and the desired thickness of the fluid level was reached. The Petri dish containing both the wafer and PDMS prepolymer was then placed in a dessicator and connected to the vacuum line until all the bubbles disappeared. After all the bubbles were gone, the Petri dish was placed in an oven set to 80°C and cured it for 30 minutes. After the curing, nylons tubes (McMater, Robbinsiville, NJ) that are to serve as reservoirs to collect the sorted carbon nanotubes were carefully placed at the desired spots of channel outlets. After the reservoirs were placed, PDMS liquid precursor mixed with 10 parts of Sylgard 184 silicone elastomer base and 1 part of Sylgard 184 silicone elastomer curing agent by weight was poured into the Petri dish as the top layer to seal the reservoirs. It is important to repeat the step of removing air bubbles in the dessicator and curing the prepolymer in the oven. The block with flow channels was cut into PDMS with the desired dimensions using a scalpel and carefully separated and peeled the PDMS block off from the silicon wafer.

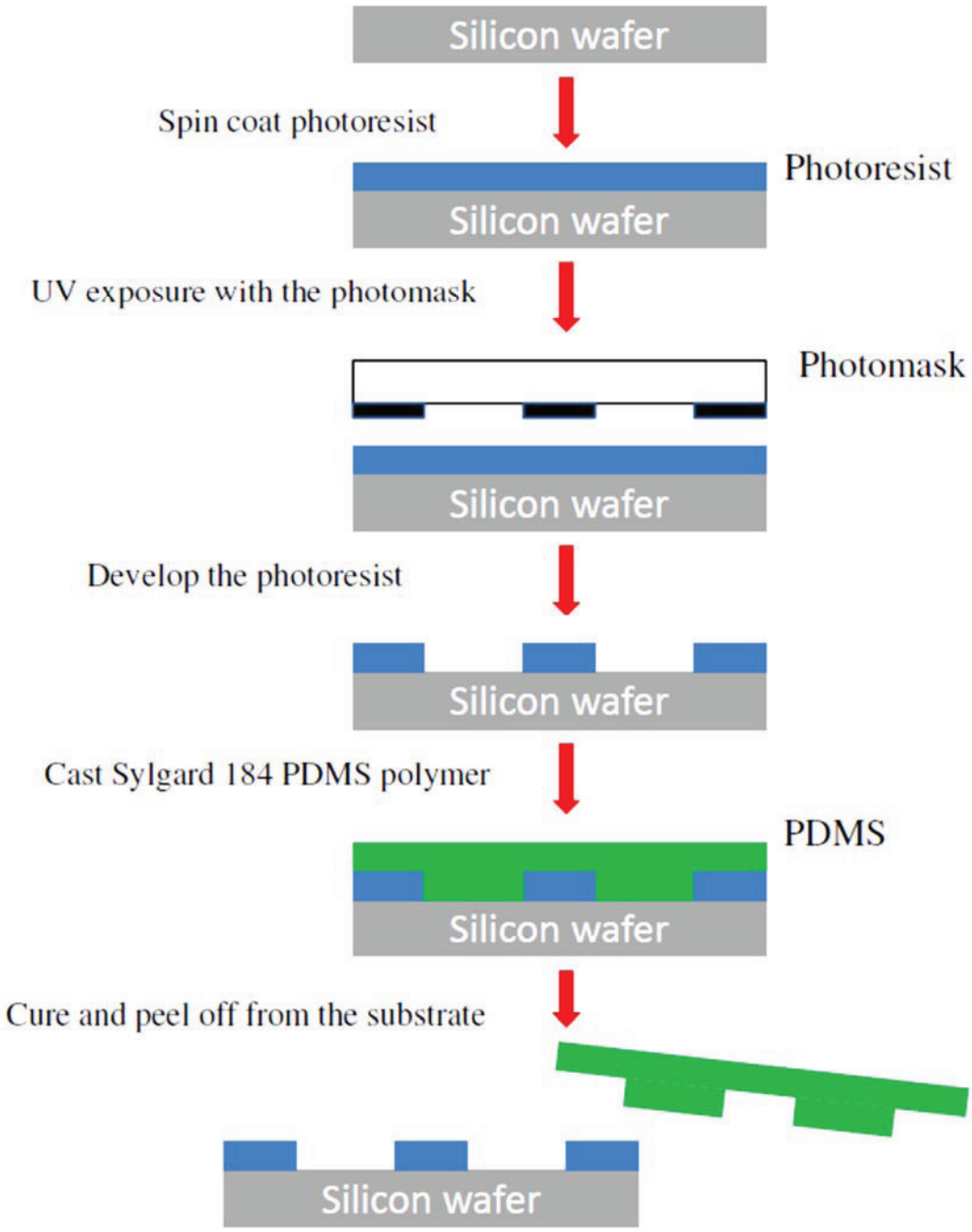

Figure 4.6 The schematic of fabricating the PDMS flow channels.

The reservoirs were then punched through at the back side of PDMS layer using a punch (Harris Uni-core, Ted Pella, Redding, CA). A double ended blunt head needle (30 Gage, ¼" in diameter, Ellsworth Adhesives) connected with a tubing (Sllastic laboratory tubing, 30 Gage, Dow Corning) was inserted into the inlet of the flow channels. The preinstalled PDMS block and the Au electrode were cleaned and rinsed with acetone and isopropyl alcohol and then blew dry with N_2 gas. The cleaned PDMS block and Au electrode were then oxygen plasma cleaned for 2 minutes. The flow channels were attached and carefully aligned with the Au electrode by pressing the PDMS block onto the surface of the glass slide. Finally, the completed flow device as shown in Figure 4.6 was connected with a syringe (10ml, BD).

Figure 4.7 The picture of a typical flow device with PDMS flow channels attached to the Au electrode. The inlet of flow channels is connected to a syringe.

Single-walled carbon nanotubes (SWCNTs) purchased from Sigma-Aldrich (carbon > 90%, ≥ 70% carbon as SWCNT) were used in this study. Suspensions were prepared by mixing 2 mg of raw SWCNTs roots in 20 ml deionized water with 1 wt.% of the surfactant sodium dodecyl sulfate (SDS) (99.0%, Sigma-Aldrich). The suspension was ultra-sonicated for 1 hour and then centrifuged at 3000 rpm for 48 hours. The upper 80% of the suspension was used in the experiment. As shown in Figure 4.8, an automated single syringe pump (Fisher Scientific) was used to push and control the flow rate of the stream of mixed SWCNTs into the microfluidic channels of the flow device. The flow rate was ~ 2 μL/min. The stream of mixed SWCNTs was experienced the AC electric field gradient generated by the BNC function generator (model 835, microwave/ RF signal generator) with 5 V_{p-p} at 500 MHz, 5 V_{p-p} at 100 MHZ. or 5 V_{p-p} at 10 MHz. Two separate reservoirs were used to catch different types of nanotubes in each as shown in Figure 4.9. An ultraviolet-visible near infrared (UV-Vis-NIR) spectroscopy (Shimadzu, UV-2600 spectrophotometer with extension) measured the absorption spectrum of metals and semiconductors in the visible to near-infrared region, using a quartz cell with a path length of 5 mm. The measurements can provide the global measurement of the relative metallic to semiconducting SWCNTs content.

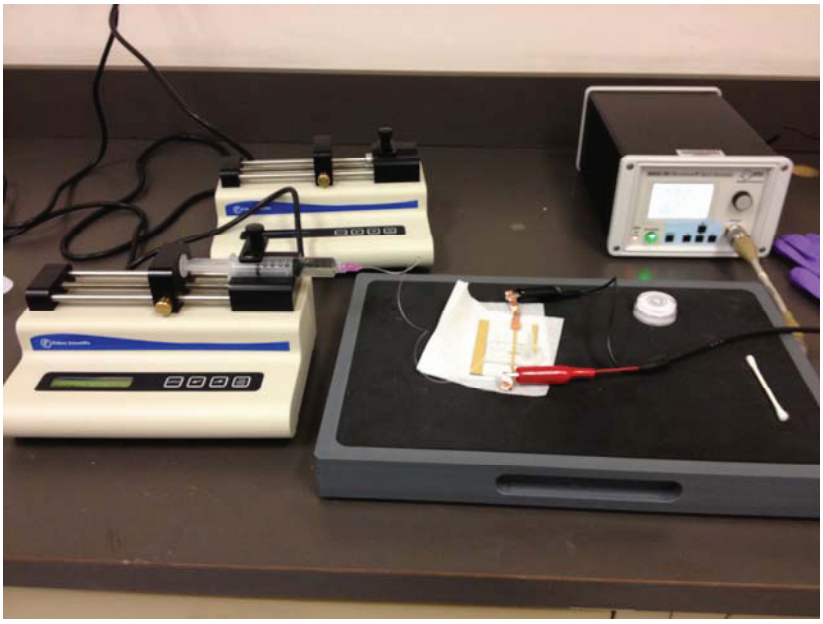

Figure 4.8 Image of the typical experimental setup for SWCNTs separation experiments.

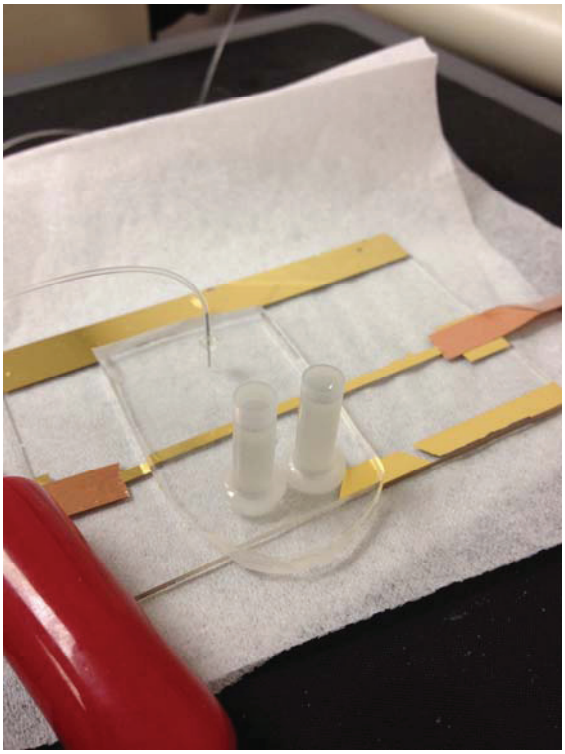

Figure 4.9 Image of the two separate reservoirs used to collect nanotubes.

4.3 Results and Discussion

4.3.1. Static System

Figure 4.3 shows positions where Raman spectra were taken. Raman spectra of SWCNTs at position 1 and position 4 are shown in Figure 4.10. Comparing the measured Raman spectra to reference Raman spectra shown in Figure 4.11 generated by Dresselhaus *et al.*, the spectra of the D and G bands from positions 1 and 4 matches well with the spectra for purified metallic tubes and purified semiconducting tubes respectively.

The radial breathing mode (RBM) region usually occurs at the frequencies of 100 to 350 cm^{-1} for SWCNTs[31] and according to Araujo *et al.* and Dresselhaus *et al.*, the RBM frequency, ω_{RBM}, is depended on the reciprocal of the carbon nanotube diameter, d_t.[10,32-34] The wavenumbers of RBM peaks also provide information on chirality, which is related to the electronic properties of SWCNTs. Li *et al.* summarized this reciprocal dependence between RBM frequency and carbon nanotube diameter is valid when the tube diameter is larger than 0.7 nm.[38] However, when the diameter of a SWCNT becomes smaller, the reciprocal dependence will become invalid due to the induced curvature effect.[38-39]

In Figure 4.10, for laser excitation energy of 2.41 eV (514 nm), the Raman spectra of SWCNTs near the semicircular outer electrode (position 4) show a sharp peak at 267 cm^{-1}. This peak indicates the possible presence of some metallic SWCNTs around the area despite the dominant semiconducting signal. The Raman profiles of SWCNTs near the circular inner electrode (position 1) do not show any peaks in the RBM region.

Instead, a flat and broad curve is revealed in this region. This may be due to a high local concentration of SDS surfactant that affects the Raman spectra at the RBM wavenumbers.

G-band mode is related to vibrations in all sp^2 carbon materials. The characteristic Raman peak of the G-band mode corresponds to the electronic properties (semiconducting or metallic) of SWCNTs.[24] In general, as shown in the reference Raman spectra in Figure 4.11, the Raman spectra of semiconducting SWCNTs show a sharp peak at 1592 cm^{-1} for the G-band mode, while metallic SWCNTs generate a broad peak at 1582 cm^{-1} for the G-band mode.[16,29,31,37,40-41] The G-band mode signal of the tubes near the semicircular outer electrode (position 4) shows a sharp peak at 1591 cm^{-1}. The G-band mode signal of the tubes near the circular inner electrode area (position 1) shows a sharp peak at 1585 cm^{-1}. The SWCNTs at position 1 are metallic after the separation experiment. At position 4, the SWCNTs show semiconducting behavior, although with some possible metallic contamination in that region.

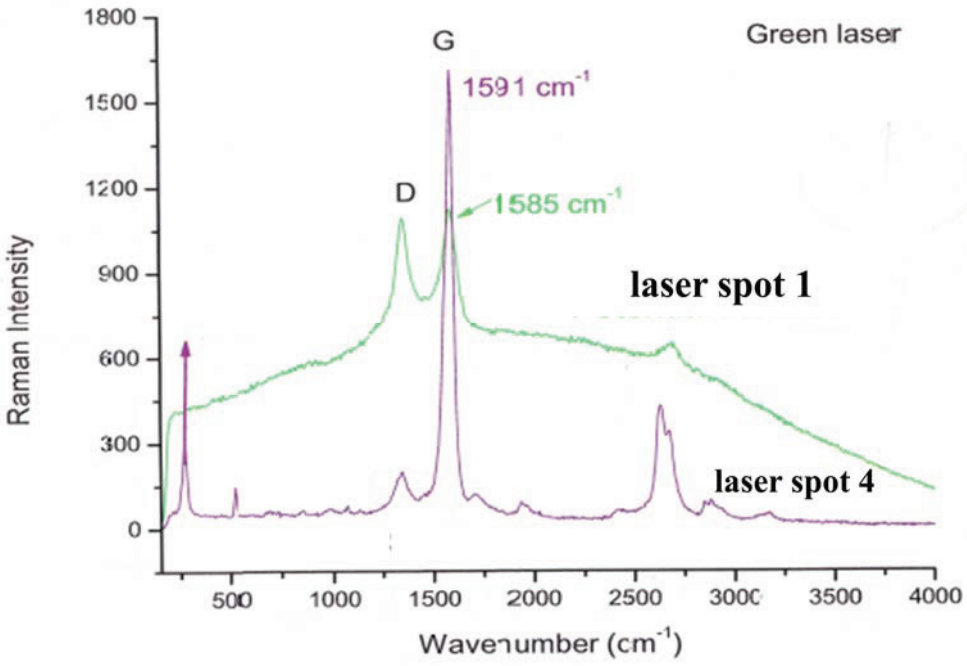

Figure 4.10 Raman spectra of SWCNTs at position 1 and 4.

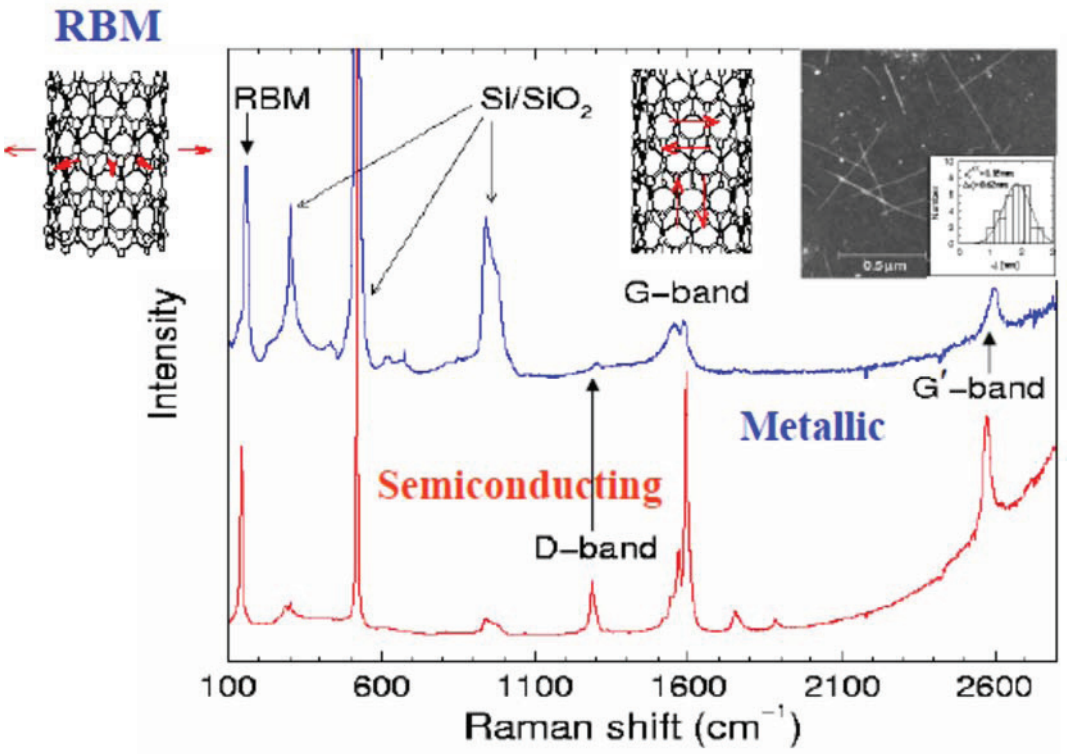

Figure 4.11 Full Raman spectra of metallic and semiconducting carbon nanotubes generated by Dresselhaus *et al*. Figure reprinted from *Raman Scattering in Carbon Nanotubes*.URL: nanotube.msu.edu/nt05/abstracts/NT05tutor-Dresselhaus.pdf. Copyright 2005, M. S. Dresselhaus.

Figure 4.12 shows normalized Raman spectra of RBM frequencies of SWCNTs that are about 5 μm away from the circular inner electrode (position 2), and about 300 μm away from the circular inner electrode (position 3). We distinguish between the metallic and semiconducting SWCNTs by their corresponding RBM frequencies. According to the Katauru plot shown in Figure 4.13, for the laser excitation energy of 2.41 eV (514 nm), the RBM frequencies of semiconducting SWCNTs are in the range of about 175 to 213 cm^{-1}, and the RBM frequencies of the metallic SWCNTs are at about 120 to 150 cm^{-1} and 218 to 280 cm^{-1}.[4,29,37,45]

Shown in Figure 4.12, two peaks at 127 cm^{-1} and 208 cm^{-1} and a double peak at 263 cm^{-1} and 271 cm^{-1} are shown in the RBM spectra. These peaks indicate the mixed metallic and semiconducting electronic types of SWCNTs in the reference sample before the separation. A peak at 249 cm^{-1} and a dominant double peak at 264 cm^{-1} and 275 cm^{-1} appear in the RBM spectra for the tubes at position 2. A peak at 249 cm^{-1} and a sharp double peak at 265 cm^{-1} and 273 cm^{-1} appear in the RBM spectra for the tubes at position 3. With the peak information in the RBM range compared to the Katauru plot with respect to a linear Raman shift axis shown in Figure 4.12, the strongly dominant intensity of RBM frequency in the range between 218 to 280 cm^{-1} shows that SWCNTs at position 2 and position 3 are dominantly purified metallic behaviors. Because a single excitation energy was used in the experiment, only nanotubes resonant with this laser energy will display peaks at corresponding frequencies.

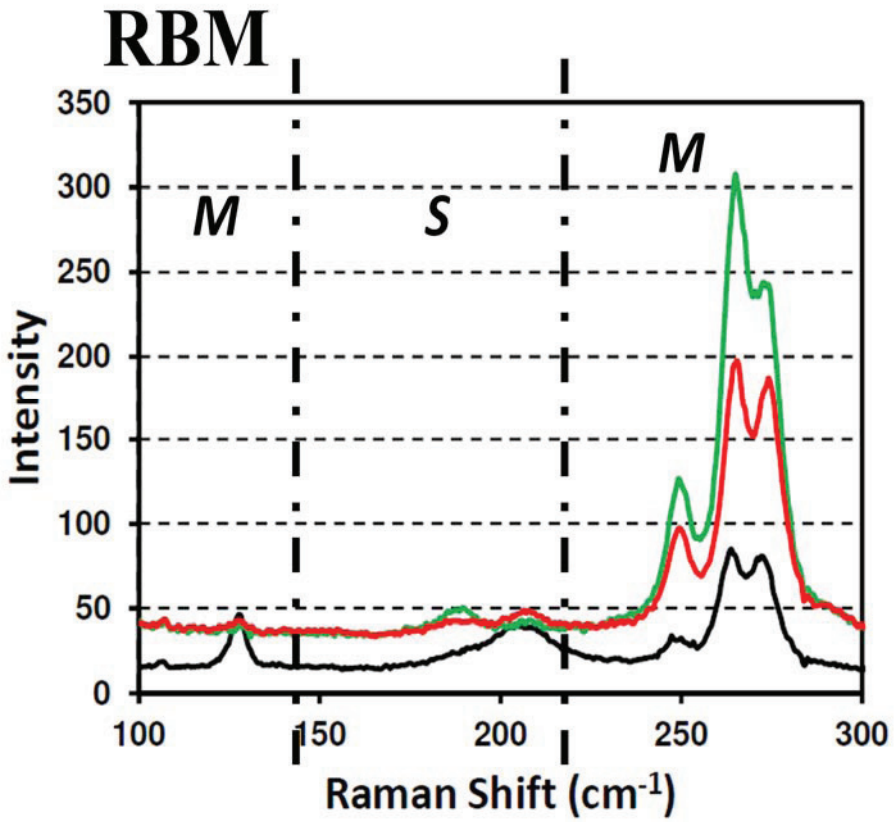

Figure 4.12 Raman spectra of radial breathing mode (RBM) frequencies of SWCNTs using the laser excitation energy of 2.41 eV (514 nm) after the separation by AC dielectrophoresis. The red dot line represents the RBM profile of the CNTs at position 2. The green line shows the RBM profile of the CNTs at position 3. The black line indicates the control sample of mixed SWCNTs before the separating experimentation.

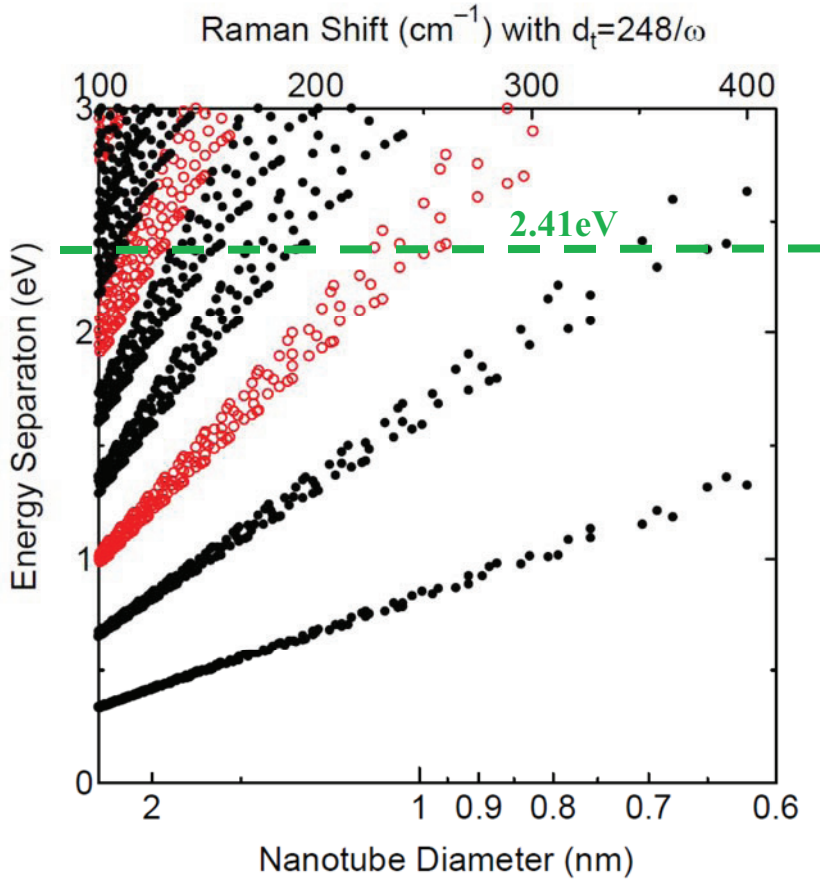

Black points are semiconductor nanotubes

Red points are metallic nanotubes

Figure 4.13 Katauru plot with respect to a linear Raman shift axis for the laser excitation energy of 2.41 eV (514 nm).[22] Figure reprinted from URL: http://www.photon.t.u-tokyo.ac.jp/~maruyama/kataura/kataura2n.pdf. Copyright 2002, Dr. S. Maruyama, University of Tokyo.

Owing to the DEP force, the metallic SWCNTs were separated from the mixture and drawn towards the circular inner electrode, while the semiconducting ones were driven toward the semicircular outer electrode under the action of an AC field. This indicated that the metallic SWCNTs experienced positive DEP force and were attracted to the high field density area when the dielectric constant of the medium (1 wt.% SDS solution) is ~ 80.[6] On the other hand, the low dielectric constant of semiconducting SWCNTs (< 5)[6] experienced a negative DEP force, causing them to move toward the low electric field density region. In this case, the higher electric field density occurs at the region of circular inner electrode, and the lower one happens at the region of semicircular outer electrode.

A physical interpretation of the results just discussed will now be given. Figure 4.14 shows the magnitude and direction of DEP force and coulombic attraction from the Au electrodes at the four measured positions. The SWCNTs within the suspension still form bundles or clusters after the ultra-sonication and centrifugation steps. Within the bundles or clusters, the metallic and semiconducting SWCNTs are randomly distributed. When the electric field is applied, the SWCNT bundles or clusters near the Au electrode are instantaneously attracted by the coulombic attraction toward the electrode, which, at this point, the coulombic attraction dominates the DEP force. Although the region is full of metallic SWCNTs, semiconducting SWCNTs can be detected by a Raman spectrometer near the circular inner electrode region. On the other hand, SWCNTs composed of semiconducting tubes with a trace amount of metallic tubes are near the semicircular outer electrode. At position (laser spot 2), although the coulombic attraction becomes weaker, the trace of semiconducting SWCNTs still appears around the region.

Separated SWCNTs around the position 3 are unique compare to other three spots. SWCNTs around position 3 experienced very little coulombic attractions from both electrodes.

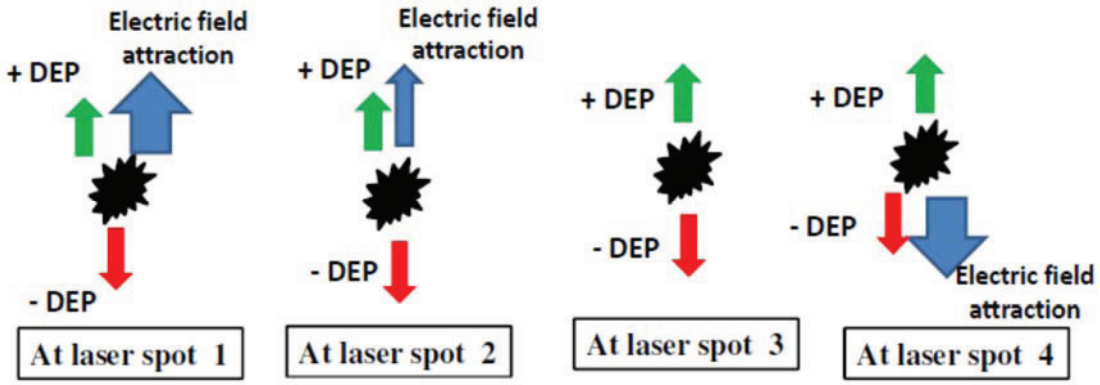

Figure 4.14 DEP force and electric field attraction at the four Raman measured positions.

4.3.2 Continuous Flow System

Adapting the initial successful results on separating two types of SWCNTs, the gradient of the electric field in the dynamic flow experiments is going to be generated by the non-uniform shape of the electrodes as shown in Figure 4.15. The work now focused on fabricating a dielectrophoretic (DEP) force utilized microfluidic lab-on-a-chip device that can continuously separate and collect a large quantity (at mg level) of metallic and semiconducting SWCNTs into two reservoirs. The high electric field region is generated at the circular shaped electrode, which has a diameter of 5 mm. The low electric field region is generated at the rectangular shaped electrode, which has a length of 10 mm and the width of 2 mm. The distance between the edge of the circular electrode to the edge of the rectangular electrode is about 0.23 mm. With the geometries and the applied AC

voltage of 5 V_{p-p} at 10 MHz, the system can generate the electric field gradient of 4.7 x 10^4 V/m as shown in Figure 4.16 simulated by ANSYS Ansoft Maxwell V12.1 software.

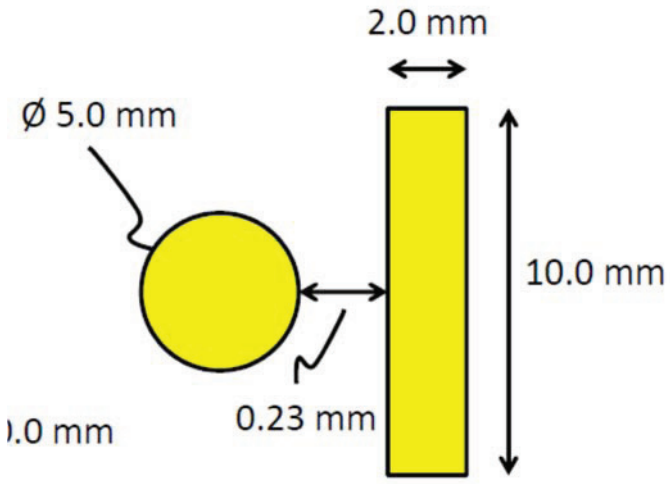

Figure 4.15 Schematic of the Au electrodes with their dimensions in the continuous flow experiments.

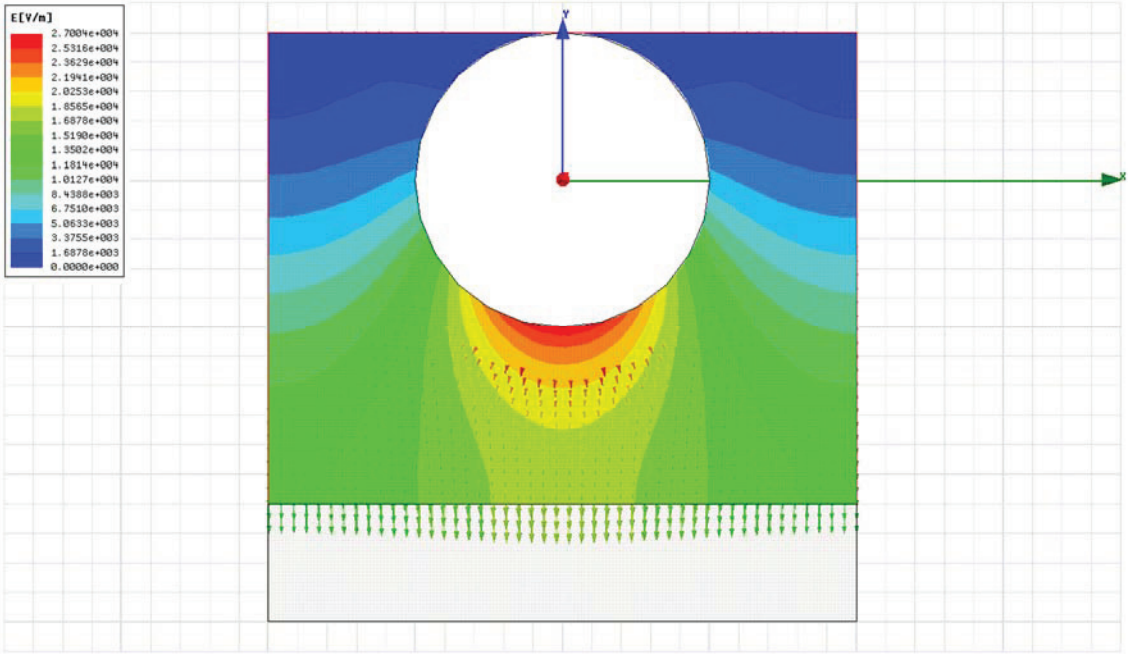

Figure 4.16 The plot of software simulated electric field gradient in the continuous flow experiments generated by the non-uniform shape of the electrodes using ANSYS Ansoft Maxwell V12.1 software.

With the flow rate of 0.12 mL/hr (0.12 mg/hr) and the generated electric field gradient of 4.7 x 10^4 V/m, the ultraviolet visible near infrared (UV-Vis-NIR) absorption spectra of aqueous suspended SWCNTs as shown in Figure 4.17 shows that purified SWCNTs are collected in the reservoir 1 and impurities such as metallic catalyst or amorphous carbon from the synthesizing process of carbon nanotubes in the reservoir 2. The UV-Vis-NIR absorption spectrum of as-received SWCNTs is also shown in the Figure 4.17 as the reference. The UV-Vis-NIR spectra provide a global measurement of the relative metal/semiconductor content compared to a local measurement from the Raman spectroscopy. In addition, all types of SWCNTs are active in UV-Vis-NIR region. The small spot size of the laser used in a Raman spectroscopy required statistical averaging over numerous measurements in order to get confident results.[46] Therefore, one cannot be sure that a truly representative result is obtained. Figure 4.18 shows the extension of UV-Vis-NIR spectra of the purified SWCNTs to confirm the existence of both metallic and semiconducting nanotubes by identifying their corresponding peak positions. The SWCNT absorption spectra exhibits sharp peaks around 900 - 1350 nm indicated the optical transition from the first valance band to the first conduction band associated with van Hove singularities of semiconducting SWCNTs.[47] The absorption peaks around 525 - 750 nm represent the first optical transition of metallic SWCNTs.[15,48,49] The presence of both types of absorption peaks indicates the existence of both metallic and semiconducting nanotubes collected in the reservoir 1 with the DEP separation happened in 5 V_{p-p} at 10 MHz DEP conditions.

Current SWCNTs growth process leads different side products of amorphous and crystalline impurities such as catalyst particles from arc-discharge technique. Certain

amount of impurities such as amorphous carbon will appear even with the cleanest chemical vapor deposition (CVD) growth process. The presence these impurities can lead the ultimate failure of SWCNT-based field-effect transistor (SWCNT-FET) devices, since the highest level of the same grade of SWCNTs is required.[46] Therefore, the demonstration of this one flow path purification from the as-received or as-grown SWCNTs is not only the first critical step before refined SWCNT sorting but also a potential scale-up process that can be adapted by the industry.

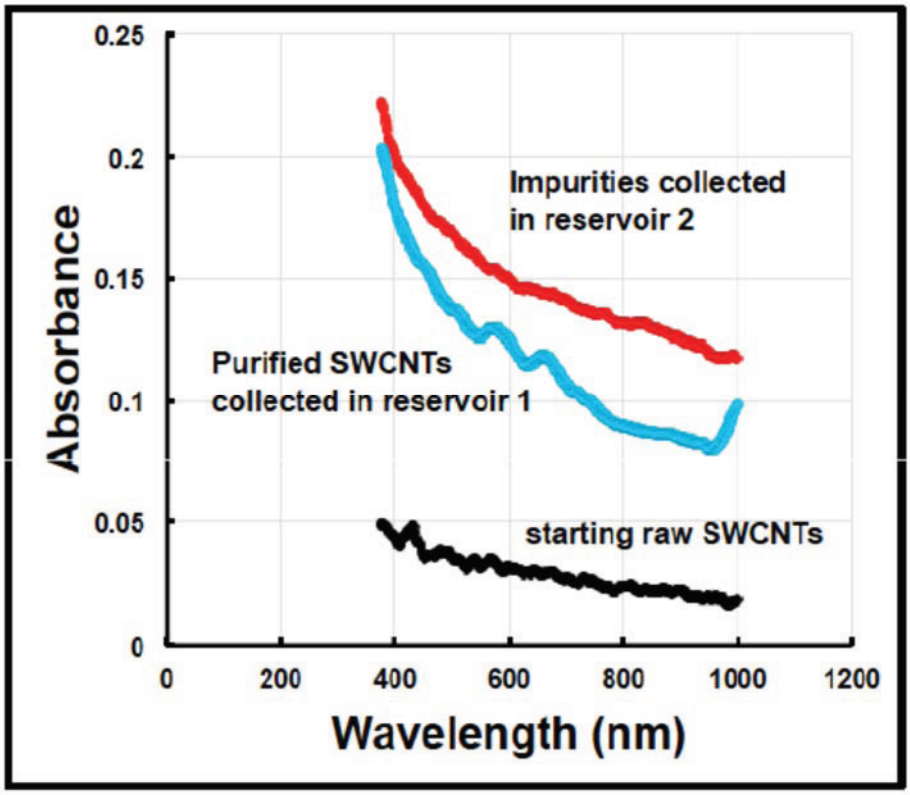

Figure 4.17 UV-Vis spectra showing purification of SWCNTs in the reservoir 1 at 5 V_{p-p} and 10 MHz DEP conditions.

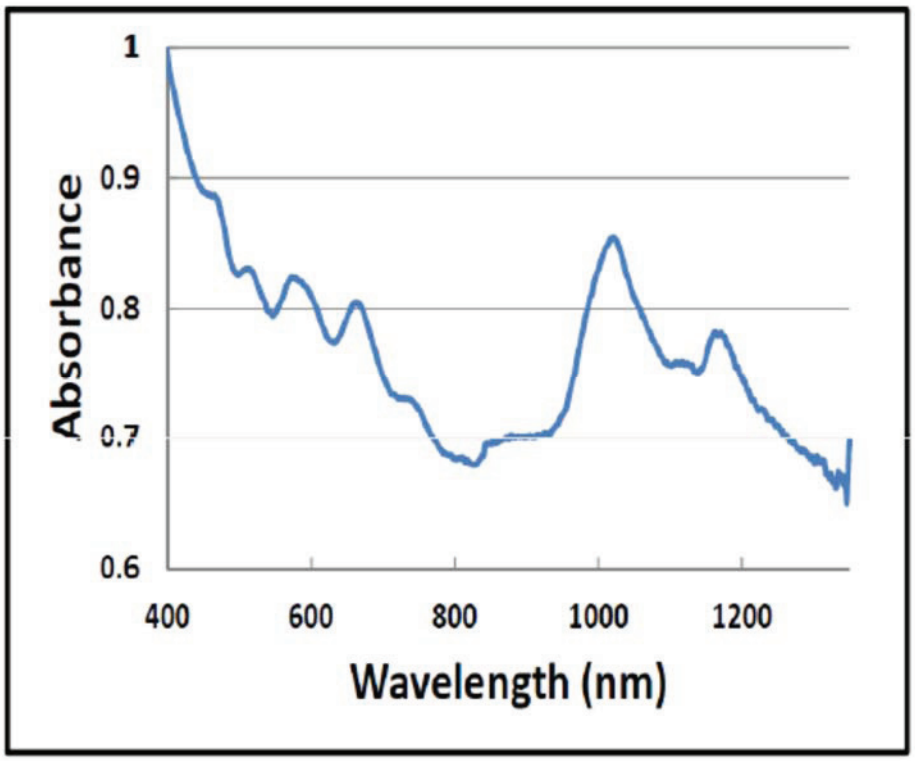

Figure 4.18 UV-Vis-NIR spectra showing the extension of purified SWCNTs in the reservoir 1 at 5 V_{p-p} and 10 MHz DEP conditions.

Furthermore, with the same electrode geometries and dimensions but applied DEP force at 500 MHz with 5 V_{p-p}, the UV-Vis-NIR spectrum (solid line plotted in red) as shown in Figure 4.19 indicates the ~ 7% increase in the purity of semiconducting SWCNTs comparing to the spectrum of the unsorted sample (dash line plotted in black). On the other hand, the UV-Vis-NIR spectrum (solid line plotted in green) of DEP condition at 100 MHz with 5 V_{p-p} displayed the ~ 3% increase in the purity of semiconducting SWCNTs comparing to the spectrum of the unsorted sample. The purity of metallic or semiconducting tubes is quantified by integrating the area under the corresponding peaks of metallic and semiconducting tubes from the UV-Vis-NIR spectra. In the mean time, there is a ~ 7% decrease in purity of metallic tubes at the DEP condition of 500 MHz with 5 V_{p-p}. This result may indicate that the possibility of ~ 7% of

metallic nanotubes trapped and attracted on the Au electrode by the stronger DEP force due to the larger electric field gradient while much pure semiconducting nanotubes are pushed into the reservoir by the flow. The absorptivities of as-received and unsorted SWCNTs are tested by the in-house UV-Vis-NIR spectroscopy to ensure the accuracy of the purity measurement. The absorptivities of unsorted tubes were 27.8% and 72.2%, respectively. The theoretical concentrations of metallic and semiconducting SWCNTs are about 33% and 67%, respectively.[47] Therefore, the good match between the measured data and the theoretical prediction indicates the reliability of the SWCNT purity measurement.

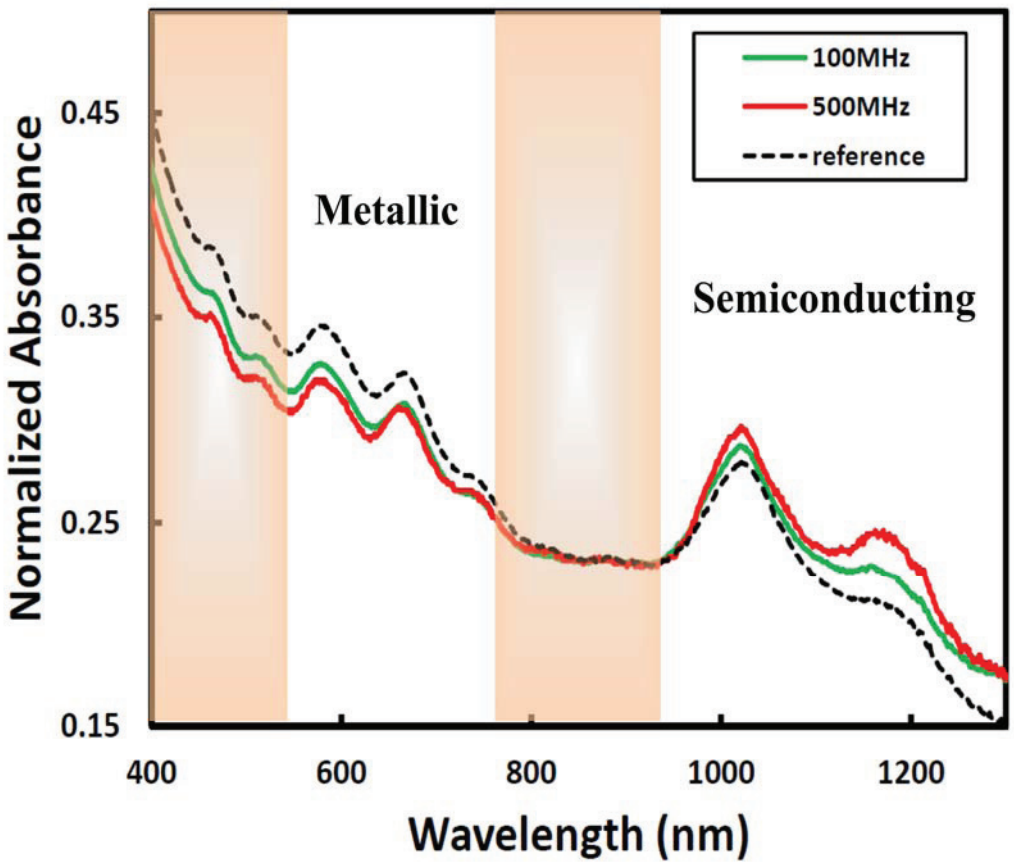

Figure 4.19 UV-Vis-NIR spectrum showing indicates the ~ 7% increase in purity of semiconducting SWCNTs in both reservoirs at the DEP of (5 $V_{p\text{-}p}$, 500 MHz) and (5 $V_{p\text{-}p}$, 100 MHz) conditions.

4.4 Conclusions

The method to separate metallic from semiconducting SWCNTs in suspension containing both types based on AC dielectrophoresis (DEP), was reported. Applying this technique in a static system, metallic SWCNTs were effectively separated from semiconducting ones due the different magnitude of dielectrophoretic forces experienced in the suspension between these two types. The significant force difference comes from a very large absolute dielectric constant of metallic SWCNTs and the low value of a finite dielectric constant of semiconducting nanotubes. It was discovered that the repulsive effect between positive and negative DEP forces is the strongest in the center portion between the circular inner electrode and semicircular outer electrode. Resonant Raman spectroscopy was used to confirm the observed results. In the dynamic flow system, the feasibility of continuously collecting purified SWCNTs with the designed flow device at 10 MHz and 5 V_{p-p} DEP conditions is demonstrated by confirming the UV-Vis-NIR spectra. Moreover, the experiment also demonstrates the feasibility of continuously collecting refined semiconducting SWCNTs with the same flow device at (500 MHz, 5 V_{p-p}) and (100 MHz, 5 V_{p-p}) DEP conditions.

4.5 Future Work

With these successful initial results, we have demonstrated that SWCNTs purification and sorting in a single pass flow system is possible. Some avenues to enhance the refinement of metallic or semiconducting SWCNTs are to optimize the flow and separation parameters. For collecting more refined semiconducting SWCNTs, the geometry of electrode could be optimized in order to create a greater electric field gradient and therefore greater DEP force. A tip shaped electrode could be substituted for the circular shaped electrode, thus enhancing the DEP force acting on the metallic tubes.

As a result, more metallic nanotubes would be attracted towards the tip-shaped electrode. Therefore, a significantly greater quantity of more refined semiconducting SWCNTs could be collected in the reservoirs. Another possibility is to collect refined metallic nanotubes by adding a channel of buffer (SWCNT-free) solution at the same constant flow rate as the mixed SWCNTs suspension in order to flush the metallic SWCNTs attached on the electrode, thus improve the purity of metallic SWCNTs collected in the reservoirs. The image of an extra buffer channeled prototype was built and is shown in Figure 4.20.

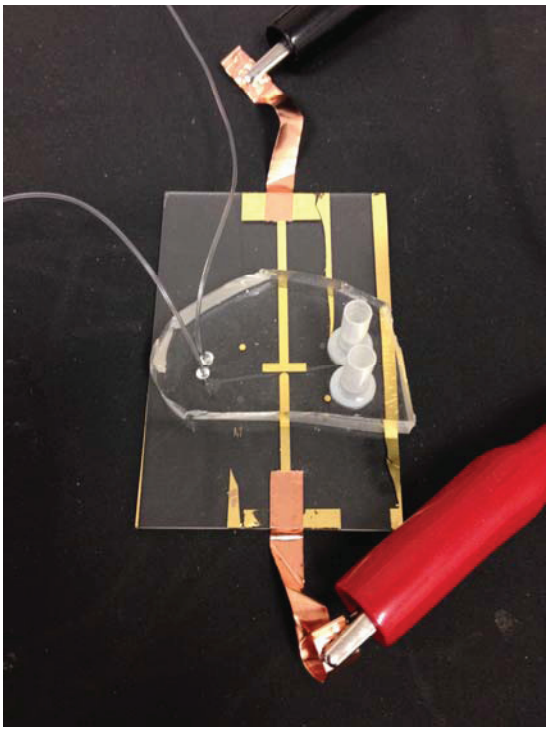

Figure 4.20 Image of an extra buffer channeled flow device used to flush the metallic SWCNTs attached on the electrode.

In addition, the geometry of flow channels may be modified to minimize the occurrence of turbulent flows inside the channels resulting in better hydrodynamic flow in order to prevent any possible remixing of already separated SWCNTs. It may be possible to improve the location of the channels with respect to the Au electrodes in order to produce better alignment during the construction of flow devices. It also may be possible to optimize the flow rate of the SWCNT suspension to allow the mixed SWCNTs sufficient time to interact with the AC electric field gradient in order to have more effective separation due to the DEP forces. The medium could be changed to adjust the permittivity and conductivity of the SWCNT suspension resulting in different magnitudes of positive and negative DEP forces compared to the current distilled water with SDS surfactant.

It would also be worthwhile to attempt multiple feeding the separated SWCNTs back to the flow system to determine the repeatability of the device and also to further purify both electronic types of SWCNTs. In addition, constructing and running a multistage flow system using multiple linked flow devices in series would be of interest as shown schematically in Figure 4.21.

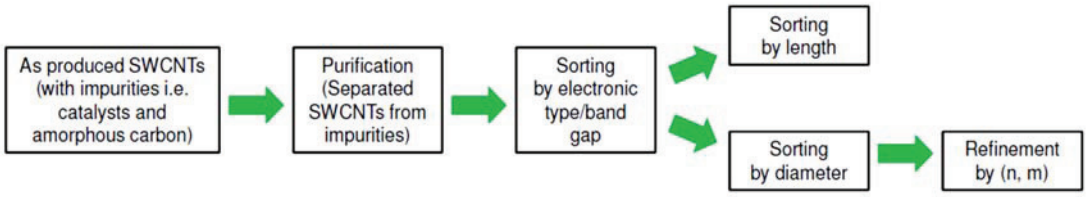

Figure 4.21 Schematic of potential future direction of the invited one-pass DEP derived flow device for sorting SWCNTs.

The discussed flow device may also open up possibilities in terms of biological material applications. For example, it would be interesting to construct a continuous flow dielectrophoretic sorting of live and dead yeast cells based on the method of I. Doh and Y. H. Cho.[50] They showed that the viable yeast cells exhibited a positive DEP force, whereas the non-viable yeast cells exhibited a negative DEP force. Using this similar idea to separate bio-entities depending on the difference in polarizability between cells and surrounding medium, our method may be able to provide a system that does not damage biological cells during separation while obtaining a throughput of tens of thousands of cells per second.

Bibliography

1. P. Avouris, Feature: Nanotube electronics, *Physics World* **20**, 40-45 (2007).
2. P. Avouris and J. Appenzeller, Electronics and Optoelectronics with Carbon Nanotubes, *The Industrial Physicist*, June/July, 18-21 (2004).
3. M. John, Exotic Carbon Molecules Offer a Promising Path To Ever Smaller Chips, page B2, New York edition, *The New York Times* (October 29th, 2012). URL: http://bits.blogs.nytimes.com/2012/10/28/i-b-m-reports-nanotube-chip-breakthrough/?_r=0
4. R. Krupke, F. Hennrich, H. v. Löhneysen, and M. M. Kappes, Separation of Metallic from Semiconducting Single-Walled Carbon Nanotubes, *Science* **301**, 344-347 (2003).
5. N. Peng, Q. Zhang, J. Li, and N. Liu, Influences of ac electric field on the spatial distribution of carbon nanotubes formed between electrodes, *J. Appl. Phys*. **100**, 024309 (2006).
6. R. Krupke, F. Hennrich, M. M. Kappes, and H. v. Löhneysen, Surface Conductance Induced Dielectrophoresis of Semiconducting Single-Walled Carbon Nanotubes, *Nano. Lett.* **3**, 1019-1023 (2003).
7. T. Tanaka, H. Jin, Y. Miyata, and H. Kataura, High-Yield Separation of Metallic and Semiconducting Single-Wall Carbon Nanotubes by Agarose Gel Electrophoresis, *Appl. Phys. Expr.* **1**, 114001 (2008).
8. Price of sorted metallic and semiconducting nanotubes. URL:http://www.sigmaaldrich.com/technical-documents/articles/materials-science/nanointegris.html

9. M. S. Dresselhaus, G. Dresselhaus, and M. Pimenta, The remarkable properties of carbon nanotubes as nanoclusters*, Eur. Phys. J. D.* **9**, 69-75 (1999).
10. M. S. Dresselhaus, G. Dresselhaus, A. Jorio, A. G. Souza Filho, and R. Saito, Raman spectroscopy on isolated single wall carbon nanotubes, *Carbon* 40, 2043-2061 (2002).
11. P. Avouris, J. Appenzeller, R. Martel, and S. J. Wind, Carbon Nanotube Electronics, *Proceedings of the IEEE* 91 (11), 1772-1784 (2003).
12. This section is an adapted reproduction from Su Chih Chi, Robert C. Cammarata, Chia-Ling Chien, Donglei Fan, Stephen Farias, and Danru Qu, inventors, Johns Hopkins University, assignee, "Systems and Methods for Separating Metallic and Nonmetallic Particles in a Mixed-Particle Suspension," U. S. Patent Provisional Application No. 13/902,191, Filling date: May 24, 2013.
13. M. S. Dresselhaus, G. Dresselhaus, and R. Saito, PHYSICS OF CARBON NANOTUBES, *Carbon* **33**, 883-891 (1995).
14. M. Ouyang, J.-L. Huang, and C. M. Lieber, Fundamental Electronic Properties and Applications of Single-Walled Carbon Nanotubes, *Acc. Chem. Res.* **35** (12), 1018-1025 (2002).
15. H. Liu, Y. Feng, T. Tanaka, Y. Urabe, and H. Kataura, Diameter-Selective Metal/Semiconductor Separation of Single-wall Carbon Nanotubes by Agarose Gel, *J. Phys. Chem. C* **114**, 9270-9276 (2010).
16. M. S. Dresselhaus, G. Dresselhaus, R. Saito, A. Jorio, Raman spectroscopy of carbon nanotubes, *Physics Reports* **409**, 47-99 (2005).

17. E. Pop, D, Mann, Q. Wang, K. Goodson, and H Dai, Thermal Conductance of an Individual Single-Walled Carbon Nanotube above Room Temperature, *Nano. Lett.* **6** (1), 96-100 (2006).

18. S. Sinha, S. Barjami, G. Iannacchione, A. Schwab, and G. Muench, Off-axis Thermal Properties of Carbon Nanotube Films, *Journal of Nanoparticle Research*, Vol. 7, Issue 6, pp 651-657 (2005).

19. S. Frank, P. Poncharal, Z. L. Wang, and W. A. deHeer, Carbon nanotube quantum resistors, *Science* **280**, 1744-1746 (1998).

20. K. Moshammer, F. Hennrich, and M. M. Kappes, Selective suspension in aqueous sodium dodecyl sulfate according to electronic structure type allows simple separation of metallic from semiconducting single-walled carbon nanotubes, *Nano Research* **2** (8), pp 599-606 (2009).

21. M. S. Dresselhaus, *Carbon Nanotubes: Synthesis, Structure, Properties, and Applications*. Springer (2001).

22. U. C. Wejinya, N. Xi, Y. Shen, and K. W. C. Lai, Modeling Dielectrophoretic Force for Manipulating Carbon Nanotubes (CNTs), 2007 IEEE/ASME International Conference on Advanced Intelligent Mechatronics. pp 1-6 (2007).

23. H. Morgan and N. G. Green, *J. Electrostatics* **42**, 279-293 (1997).

24. H. Morgan and N. G. Green, AC Electrokinetics: Colloids and Nanoparticels, Research Studies Press Ltd, 2003.

25. J. E. Kim and C. S. Han, Use of dielectrophoresis in the fabrication of an atomic force microscope tip with a carbon nanotube: a numerical analysis, *Nanotechnology* **16**, 2245-2250 (2005).

26. H. A. Pohl, *Dielectrophoretic*, Cambridge, UK (1978).

27. T. Lutz and K. J. Donovan, Macroscopic scale separation of metallic and semiconducting nanotubes by dielectrophoresis, *Carbon* **43**, 2508-2513 (2005).

28. C. Wei, T.-Y. Wei, and F.-C. Tai, The characteristics of multi-walled carbon nanotubes by a two-step separation scheme via dielectrophoresis, *Diamonds and Related Materials* **19**, 573-577 (2010).

29. D. S. Lee D. W. Kim, H. S. Kim. S. W. Lee, S. H. Jhang, Y. W. Park, and E. E. B. Campbell, Extraction of semiconducting CNTs by repeated dielectrophoretic filtering, *Appl. Phys. A* **80**, 5-8 (2005).

30. H. K. Schmidt, H. Peng, M. J. Mends, and M. Pasquali, Flow Dielectrophoretic Separation of Single Wall Carbon Nanotubes, United States Patent Application Publication, Pub. No.: US2009/0283405 A1, Pub. Date: Nov. 19, 2009.

31. A. Jorio, R. Saito, J. H. Hafner, C. M. Lieber, M. Hunter, T. McClure, G. Dresselhaus, and M. S. Dresselhaus, Structural (*n, m*) Determination of Isolated Single-Wall Carbon Nanotubes by Resonant Raman Scattering, *Phys. Rev. Lett.* **86** (6), 1118-1121 (2001).

32. M. S. Dresselhaus and P. C. Eklund, Phonons in carbon nanotubes, *Adv. Phys.* **49** (6), 705-814 (2000).

33. P. T. Araujo, A. Jorio, M. S. Dresselhaus, K. Sato, and R. Saito, Diameter Dependence of the Dielectric Constant for the Excitonic Transition Energy of Single-Wall Carbon Nanotubes, *Phys. Rev. Lett.* **103,** 146802 (2009).

34. P. T. Araujo, O. Maciel, P. B. C. Pesce, M. A. Pimenta, S. K. Doorn, H. Qian, A. Hartschuh, M. Steiner, L. Grigorian, K. Hata, and A. Jorio, Nature of the constant

factor in the relation between radial breathing mode frequency and tube diameter for single-walled carbon nanotubes, *Phys. Rev. B* **77**, 241403(R) (2008).

35. S. M. Bachilo, M. S. Strano, C. Kittrell, R. H. Hauge, R. E. Smalley, and R. B. Weisman, Structure-Assigned Optical Spectra of Single-Walled Carbon Nanotubes, *Science* **298**, 2361-2366 (2002).
36. S. Costa, E. Borowiak-Palen, M. Kruszyňska, A. Bachmatiuk, and R. J. Kaleńczuk, Characterization of Carbon Nanotubes by Raman Spectroscopy, *Materials Science-Poland* **26**(2), 433-441 (2008).
37. J. L. Sauvajol, E. Anglaret, S. Rols, and L. Alvarez, Phonons in single wall carbon nanotube bundles, *Carbon* **40**, 1697-1714 (2002).
38. I. L. Li, G. D. Li, H. J. Liu, C. T. Chan, and Z. K. Tang, Chirality-dependent curvature effect in smallest single-walled carbon nanotubes, *Appl. Phys. Lett.* **82**, 1467 (2003).
39. D. Sánchez-Portal, E. Artacho, J. M. Soler, A. Rubio, and P. Ordejón, Characterization methods of carbon nanotubes, *Phys. Rev. B* **59**, 12768 (1999).
40. M. S. Dresselhaus*, Raman Scattering in Carbon Nanotubes* (2005). URL: nanotube.msu.edu/nt05/abstracts/NT05tutor-Dresselhaus.pdf
41. M. A. Pimenta, A. Marucci, S. A. Empedocles, M. G. Bawendi, E. B. Hanlon, A. M. Rao, P. C. Eklund, R. E. Smalley, G. Dresselhaus, and M. S. Dresselhaus, Raman modes of metallic carbon nanotubes, *Phys. Rev. B* **58**, R16016-16019 (1998).

42. S. K. Doorn, M. J. O'Connell, L. Zheng, Y. T. Zhu, S. Huang, and J. Liu, Raman Spectral Imaging of a Carbon Nanotube Intramolecular Junction, *Phys. Rev, Lett.* **94**, 016802 (2005).
43. H. Kuzmany, B. Burger, A. Thess, and R. E. Smalley, Vibrational spectra of single wall carbon nanotubes, *Carbon* **36**(5-6), 709-712 (1998).
44. H. Kataura, Y. Kumazawa, Y. Maniwa, I. Umezu, S. Suzuki, Y. Ohtsuka, and Y. Achiba, optical Properties of Single-Wall Carbon Nanotubes, *Synthetic Metals* **103**, 2555-2558 (1999).
45. Katauru plot with respect to a linear Raman shift axis. URL: http://www.photon.t.u-tokyo.ac.jp/~maruyama/kataura/kataura2n.pdf
46. P. Chaturvedi, P. Verma, A, Singh, P. K. Chaudhary, H. Basu, and P. K. Basu, Carbon Nanotube-Purification and Sorting Protocols, *Defence Science Journal* **58**(5), 591-599 (2008).
47. M. S. Strano, C. A. Dyke, M. L. Usrey, P. W. Barone, M. J. Allen, H. Shan, C. Kittrell, R. H. Hauge, J. M. Tour, R. E. Smalley, Electronic Structure Control of Single-Walled Carbon Nanotube Functionalization, *Science* **301**(5639), 1519-1522 (2003).
48. M. S. Strano, Probing chiral selective reactions using a revised Kataura plot for the interpretation of single-walled carbon nanotube spectroscopy, *J. Am. Chem. Soc.* **125**, 16148-16153 (2003).
49. M. S. Arnold, A. A. Green J. F. Hulvat, S. I. Stupp, and M. C. Hersam, Sorting carbon nanotubes by electronic structure using density differentiation, *Nature Nanotechnology* **1**, 60-65 (2006).

50. I. Doh and Y. H. Cho, A continuous cell separation chip using hydrodynamic dielectrophoresis (DEP) process, *Sensors and Actuators A* **121**, 59-65 (2005).

Chapter 5

Summary

In this Final chapter, the author would like to summarize the previous discussions. In the first chapter, the author described the feasibility of electrodepositing pure lanthanum and lanthanum telluride compounds in ambient conditions are demonstrated. Scanning electron microscope (SEM) images showed that surface morphologies of the deposited films varied from needle-like to granular structures depending on the deposition conditions. Many nanostructured surface features on the electrodeposited samples may enhance ZT because the appearance of a large numbers of grain boundaries can scatter phonons more effectively than electrons resulting in a lowering of the thermal conductivity. The measured Seebeck coefficients and electrical resistivity of the electrodeposited thin films were closely matched to the state-of-the-art thermoelectric properties of bulk samples synthesized by mechanical alloying and the hot-press sintering. The calculated power factor of the deposited films was ranged from 8.1 x 10^{-5} to 28.5 x 10^{-5} (W m^{-1} K^{-2}). The X-ray diffraction pattern and the energy dispersive X-ray (EDAX) composition analysis of electrodeposited $La_{3-x}Te_4$ films indicated that the samples are phase pure materials.

In the second chapter, the author has shown using electrodeposition to fabricate vertically-aligned gold nanowires on a gold substrate. Scanning electron microscope (SEM) images show the gold nanowire arrays were highly dense and strongly attached to

the gold substrate after dissolution of the nanoporous anodic aluminum oxide (AAO) template. Gold nanowire arrays ferromagnetic composite films were synthesized for the first time by evaporation or electrodeposition to embed gold nanowires in nickel matrices and by electrodeposition to grow iron matrices around the gold nanowires. The electrodeposition technique preserved the spacing of the exposed gold nanowires better than the electron beam evaporation technique does. For both techniques, the density of gold nanowires across the nickel and iron matrices was homogenous regardless of the fabrication parameters.

In Chapter 3, the author has presented a novel and relatively simple approach for the synthesis of nanochanneled metal membranes with different pore sizes and inter-pore distance. Nickel nanoporous membranes of thickness less than about 0.7 μm were produced by physical vapor deposition of nickel overlayers by either electron beam evaporation or sputtering onto anodic aluminum oxide nanoporous substrates with vertically aligned nanochannels. The resulting overlayers were nanoporous, with the nanopores in the form of nanochannels aligned with the nanochannels of the substrate. In the case of the evaporated membranes, the pores had diameters within a factor of 2.5 of that of the substrate (100 nm) and a similar planar density, suggesting that the substrate acted as a template for the nanoporous nickel. The sputtered nickel also was deposited as a nanoporous material, but with a greater density of pores and smaller pore diameters, suggesting partial filling and incomplete agglomeration within the initially formed pores. For sputtered overlayers of thickness 0.7 μm or greater, the deposited metal became continuous, and electrochemical etching through the nanoporous anodic aluminum oxide (AAO) substrate was used to on these samples to produce the nanochannels. For all of

the samples, the substrate could be completely dissolved, resulting in free-standing metallic membranes.

In the fourth chapter, the author has reported a patented microfluidic device that can continuously purify and refine mixed electronic types of single-walled carbon nanotubes (SWCNTs) into separated reservoirs of metallic SWCNTs and semiconducting ones, respectively. Based on AC dielectrophoresis (DEP) in a static system, metallic SWCNTs are effectively separated from semiconducting ones due the different magnitude of dielectrophoretic forces experienced in the suspension between these two types. The significant force difference comes from a very large absolute dielectric constant of metallic CNTs and the low value of a finite dielectric constant of semiconducting nanotubes. It is discovered that the repulsive effect between positive and negative DEP forces is the strongest in the center portion between the circular inner electrode and semicircular outer electrode. Resonant Raman spectroscopy is used to confirm the observed results. In the dynamic flow system, the feasibility of continuously collecting purified SWCNTs with the designed flow device at 10 MHz and 5 V_{p-p} DEP conditions is demonstrated by confirming the UV-Vis-NIR spectra. Moreover, the experiment also demonstrates the feasibility of continuously collecting refined semiconducting SWCNTs with the same flow device at 500 MHz and 2 V_{p-p} DEP conditions.

A List of Publications and Patents

1. Su Chih Chi, Stephen L. Farias, and Robert C. Cammarata, "Synthesis of Vertically Aligned Gold Nanowire-Ferromagnetic Metal Matrix Composites" *ECS Trans.* 2012 **41**(35): 119-122; doi: 10.1149/1.3699386.
2. Su (Ike) Chih Chi, Stephen L. Farias, and Robert C. Cammarata, "Fabrication of Lanthanum Telluride Thin Films Electrochemical Deposition in Ambient Conditions," *Mater. Res. Soc. Symp. Proc.* Vol. **1543** (2013).
3. Su Chih Chi, Robert C. Cammarata, Chia-Ling Chien, Donglei Fan, Stephen Farias, and Danru Qu, inventors, Johns Hopkins University, assignee, "Systems and Methods for Separating Metallic and Nonmetallic Particles in a Mixed-Particle Suspension," U. S. Patent Provisional Application No. 13/902,191, Filling date: May 24, 2013.

A List of Conference Presentations and Poster Sessions

1. Su (Ike) Chih Chi, Stephen L. Farias, and Robert C. Cammarata, A Novel Approach to Synthesize Lanthanum Telluride Thermoelectric Materials, Materials Research Society Fall Meeting, Boston, MA USA, December 3, 2013.
2. Su (Ike) Chih Chi, Stephen L. Farias, and Robert C. Cammarata, A Novel Approach to Synthesize Lanthanum Telluride Thermoelectric Materials in Ambient Conditions, Materials Research Society Spring Meeting, San Francisco, CA USA, April 3, 2013.
3. Su (Ike) Chih Chi, Stephen L. Farias, and Robert C. Cammarata, APS March Meeting, A Novel Approach to Synthesize Lanthanum Telluride Thermoelectric Thin Films in Ambient Conditions, Baltimore, MD USA, March 21, 2013.
4. Su (Ike) Chih Chi, Xuan Jiang, Danru Qu, Stephen L. Farias, SunXiang Huang, Deng Pan, C. L. Chien, Hai-Quan Mao, and Robert C. Cammarata, Precise Manipulation of Gold Nanowires as Gene Delivery Vehicles, Materials Research Society Fall Meeting, Boston, MA USA, November 29, 2011.
5. Su (Ike) Chih Chi, Stephen L. Farias, Konrad Bussmann, Joshua D. Caldwell, Danru Qu, Mingen Li, C. L. Chien, and Robert C. Cammarata, Synthesis and Magnetic Properties of Ordered, Vertically-Aligned Au Nanowire Composites and Ferromagnetic Nanochanneled Membranes, 220th Electrochemical Society Meeting, Boston, MA USA, October 10, 2011.
6. Su (Ike) Chih Chi, SunXiang Huang, Danru Qu, Nicholas Dee, Korey Kam, XingYu Liu, C. L. Chien, Hai-Quan Mao, and Robert C. Cammarata, Precise Manipulation of

Nanowires as Delivery Vehicles in Cellular Environments, Institute for NanoBio Technology Annual Symposium Poster Session, Baltimore, MD USA, May 2011.